UNIVERSITY OF CALIFORNIA SAN DIEGO

A Stokes parameter study of collagen and polycaprolactone with polarized light microscopy

A Thesis submitted in partial satisfaction of the requirement for the degree of Master of Science

in

Materials Science and Engineering

by

Aniket S Puri

Committee in charge

Professor Lisa V, Poulikakos, Chair
Professor Jon Pokorski
Professor Lingyan Shi

The thesis of Aniket S Puri is approved and acceptable in quality and form for publication on microfilm and electronically.

University of California San Diego

2021

DEDICATION

This thesis is dedicated to the memory of my dear friend Prashant Dubey (April 1996 – Dec 2016) who has brought joy to my life and whose support continues to inspire and motivate me through my life. Until next time my friend.

TABLE OF CONTENTS

LIST OF FIGURES

LIST OF TABLES

LIST OF SUPPLEMENTAL FILES/VIDEOS

ACKNOWLEDGEMENT

Firstly, I would like to thank Professor Poulikakos for being an amazing mentor. I would like to thank the professor for providing me with the opportunity to be a part of this amazing project and mentoring me through the difficult times of the pandemic. I would also like to thank professor Poulikakos for helping me grow as a researcher, being patient with me and for all the encouragement and support. I am extremely grateful for the knowledge that was imparted to me during these times and the support and understanding when things didn't go well. I would like to thank my fellow lab members Zaid and Jebin for their input. I would like to thank everybody from Poulikakos lab for being an amazing group of colleagues and fostering a great community filled with excitement, commitment and happiness.

I would like to thank Professor Jon Pokorski, Professor Lingyan Shi for agreeing to be on my thesis committee. I would like to thank professor Poulikakos for heading the committee.

Thank you to my sister Aditi for being the best sister to me, my family for letting me chase my dreams, their support and love. I would also like to thank all of my friends for their support Avinash for brainstorming ideas and helping me figure out the MATLAB portions, Andy and Suryansh for the fun times during my masters and Krutarth for the support during the pandemic.

Lastly, I would like to thank Professor Karthik Chetan V for mentoring me and providing me with the opportunity to pursue research during my undergraduate studies.

Section 2, in part has been submitted for submission for publications of the materials as it may appear in *Advanced Optical Materials*, 2021, Eric S. A. Goerlitzer; Aniket S Puri; Jebin J. Moses; Lisa V. Poulikakos; Nicolas Vogel.

ABSTRACT OF THE THESIS

A Stokes parameter study of collagen and polycaprolactone with polarized light microscopy

by

Aniket S Puri

Master of Science in Materials Science and Engineering

University of California San Diego, 2021

Professor Lisa V. Poulikakos, Chair

In this study, we demonstrate the use of Stokes polarimetry in combination with polarized light microscopy as a powerful tool in the characterization of anisotropic polymeric materials including collagen and poly (ϵ-caprolactone) fibers. Structural anisotropy has been shown to translate to optical anisotropy in the form of birefringence. We demonstrate that polarized light microscopy and Stokes polarimetry can be used to enhance the visualization of fibrous structures that are not ordinarily accessible by conventional microscopy techniques, by leveraging the birefringence of the material. With polarized light microscopy, we show the existence of birefringent Maltese cross structures in collagen synthesized at 22 ^{0}C and perform structural analysis of the system using Stokes polarimetry. The highly fibrous microstructural arrangements

observed by polarized light microscopy and Stokes polarimetry for collagen synthesized at 40 ^{0}C and poly (ϵ-caprolactone) fibers can provide insights into the kinetics of polymerization. We also observe a change in birefringence due to the effect of strain on super elastic poly (ϵ-caprolactone) fibers. Overall, we demonstrate that combining Stokes polarimetry and polarized light microscopy has the potential to provide quantitative, point by point structural analysis of fibrous biomaterials. This study holds potential to provide insights into the kinetics and mechanics of disease progression and polymer synthesis.

1. Introduction

Microscopy is a powerful tool used to characterize morphology of samples across various disciplines. Microscopy techniques most broadly can be classified into electron microscopy, optical microscopy and confocal/nonlinear optical microscopy techniques. The electron microscopy technique variants provide very high resolution[1,2] (~ 0.2 nm) but they need sample preparation involving metallic sputtering, cryopreservation, freeze drying, chemical fixation etc.[2] Even with the sample preparation, the SEM techniques still face the challenges of not accurately being able to visualize the required environment or artefacts introduced due to sample preparation in certain cases.[2–4] Confocal microscopy techniques are most widely used for imaging biological samples. The nonlinear optical microscopy techniques like multi photon microscopy[5–7], second harmonic generation microscopy[8–10], coherent anti-Stokes Raman scattering microscopy[11] are a few of the techniques that can provide very high-quality information about cellular functions and structure in this category as well. However, these techniques are significantly specialized, expensive, slower and need trained personnel for operation.[12,13] Another set of challenges faced by these techniques is related to sample preparation, requirement of tags, photobleaching and phototoxicity depending on the choice of microscopy technique and sample of interest.[12] The simple light illuminated microscopy techniques are fast, cheaper and can be used on most samples and are most widely used microscopy technique.[14] However, these microscopy techniques suffer from a subpar quality in regards to resolution[15] and lower available magnification.[16] As a result, there is a need of microscopy technique that is easily accessible to the researchers while providing high quality imaging. In recent years polarized light microscopy as a modification to the optical microscopy has proven to

be a very powerful technique in measuring anisotropic polymeric materials which would potentially improve the optical microscopy while preserving the advantage of rapid characterization for biological samples.

Most biological materials exhibit some sort of anisotropy due to their structural organization. Biological materials such as actin[17], myosin[18], fibronectin[19], collagen[8,10], laminin[20] are anisotropic due to the linear nature of hierarchical organization. These fibrous materials are responsible for building the native tissues. Most cellular organizations are a result of membrane formation due to the aligned organization of lipids resulting in anisotropy. The structural anisotropy in materials can act as a diagnostic tool in case of various diseases where the organization of these materials is influenced by the disease. For example, the order and disorder in lipids is correlated with for diseases like Alzheimer's through the formation of amyloid plaques[21–23]. Collagenous organization can lead to diseases related to fibrosis[24–26] and cancer[27,28]. The collagenous organization also plays a critical role in ocular diseases like myopia[29], glaucoma[30] and keratoconus; dermal diseases like Scleroderma[31,32] and various skin cancers[8,10,33]. The current state of the art for the characterization of the anisotropic biomaterials involves the confocal/nonlinear optical microscopy techniques. Multi photon laser scanning microscopy (MPLSM) and second harmonic generation microscopy have been used for characterization of carcinogenic tissues.[9,10,34]. However as discussed earlier, these techniques are expensive and highly specialized for microscopy as compared to simple optical light microscopy.

The structural anisotropy in most materials translates to optical anisotropy by the means of optical properties like birefringence and diattenuation. The primary observable phenomenon from

microscopy perspective is birefringence. Birefringence is a property that has been explored extensively for crystallographic characterization in the field of geology[35,36] and food sciences for starch granules[37], protein fibrils and fat crystals[38,39]. For polymers, the source of the birefringence property is two-fold. First is from the organization perspective where alignment plays a role in the interference and the second is from the molecular perspective where the semi-crystallinity and material affects the inherent birefringence of the material. The current state of the art for characterization of these properties are X-ray crystallography techniques like X-ray diffraction, small angle X-ray scattering (SAXS) and wide-angle X-ray scattering (WAXS) and thermal characterization using differential scanning calorimetry (DSC) or mechanical using dynamic mechanical analyses as well as spectroscopic techniques. These techniques are bulk characterization techniques and it is difficult to provide point by point structural analysis of the material. Using polarized light microscopy as a supplement to these characterization techniques could provide spatial information that is generally not accessible in the analysis.

An alternative set of techniques involving Mueller calculus and Jones calculus have been used to carry out the material characterization for measurement of optical properties like retardance, diattenuation and depolarization [40–42]. Efforts have also been made to enhance the birefringence of the materials using picrosirius red stains and Congo red stains to enhance the birefringence of the material for better imaging. However, the Mueller matrix of turbid media is a comparatively complex technique and requirement of either highly specialized instruments[43] or a tedious way of taking measurements[41] with specific optical retardation units. The resulting matrices are also difficult to decipher and not as easily accessible to researchers due to the validation being done by using complex simulations.[40–42,44] Additionally, enhancement of birefringence using the dyes like Congo red and Picrosirius red might prove to interfere with the

characterization of the material of choice and is dependent on the skills of the researcher performing the staining.[45,46]. Therefore, a label free method of rapid imaging is needed for characterization of the anisotropic structural material.

In this study, we show a potential use of polarized light microscopy as a tool for assessing the structural parameters and material properties that are not as easily accessible by using conventional microscopy. The microscopy setup can be used for assessing the structure, kinetics, assembly and in some cases crystallinity of the material in a rapid label free form. The Stokes polarimeter setup has been used for diagnosing diseases in the past and our findings for synthesized collagen and poly(ϵ-caprolactone) structures have a broader potential in understanding the formation of the diseases.

2. Optics theory

2.1 Introduction to polarized light

In 1892, Fresnel described light as two orthogonal disturbances. These disturbances we now know to be the orthogonal electric field of a propagating light. The light propagation in time and space can be described using the electric field component in equation 1.

$$E(z,t) = E_{0x}\, cos(\omega t - kz + \delta_x)\hat{\imath} + E_{0y}\, cos(\omega t - kz + \delta y)\hat{\jmath} \qquad \text{Eq 1}$$

Where $E_x(z,t)$ is the optical field component in xz plane, $E_y(z,t)$ is the optical field component in the yz plane, ω is the angular frequency, k is the wavenumber and δ_x and δ_y are the phase components respectively.

While eq 1 describes the polarization state of light it does not provide adequate information relating to the characteristics of the polarization state. To get a characteristic equation, it is further modified to eliminate the time dependent t and space dependent x to obtain equation 2[47,48].

$$\frac{E_x(z,t)^2}{{E_{0x}}^2} + \frac{E_y(z,t)^2}{{E_{0y}}^2} - \frac{2E_x(z,t)\,E_y(z,t)}{E_{0x}\,E_{0y}} cos\delta = sin^2\delta \qquad \text{Eq 2}$$

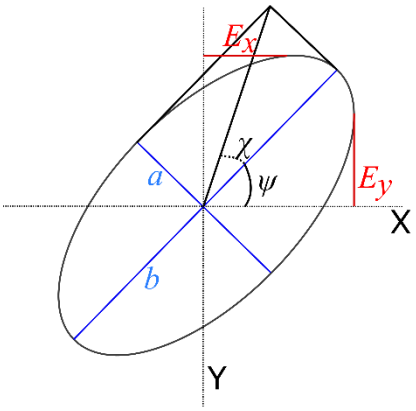

Figure 2.1 : Polarization ellipse.

The equation 2 is an equation of an ellipse in its nonstandard form. This non-standardized ellipse describes the polarization state of light and is known as the polarization ellipse shown in figure 2.1.

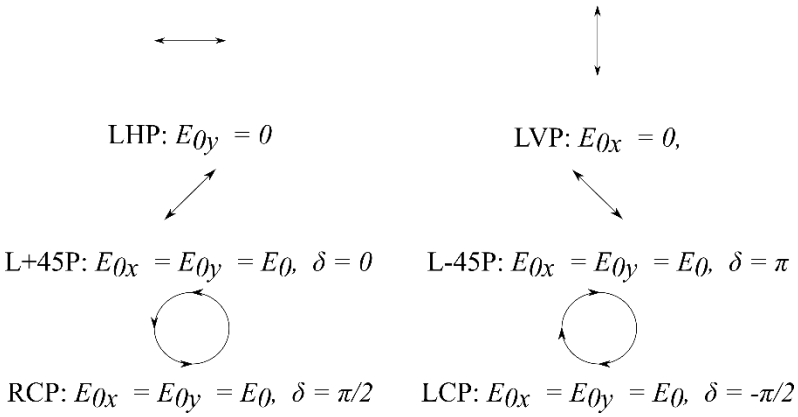

Figure 2.2: Degenerate states of light

The polarization ellipse will represent a polarization state. A set of polarization states known as the degenerate polarization states are described and labelled in the Figure 2.2[49]. The degenerate states are linear horizontally polarized light (LHP), linear vertically polarized light (LVP). The LHP and LVP can be obtained by having either $E_{0x} = 0$ or $E_{0y}=0$ respectively. The linearly polarized light at $+45^0$ (L+45P) and -45 (L-45P) can be described by $E_{0x}=E_{0y}$ and $\delta = 0$

and δ = pi respectively. The circularly polarized light can be described by making $E_{0x} = E_{0y}$. The circularly polarized light can be either right circularly polarized (RCP) at $\delta = \pi/2$ or left circularly polarized (LCP) at $\delta = -\pi/2$.

From the elliptical representation of the polarization state of light we can conclude that the polarization state of light can be described by the two characteristic quantities of ellipse. First the orientation angle ψ and second the ellipticity angle χ. These parameters can be related to the previously described parameters as shown in eq 3 and 4[47,49] respectively.

$$tan2\psi = \frac{2E_{0x}E_{0y}}{{E_{0x}}^2 - {E_{0y}}^2} cos\delta, \quad 0 \leq \psi \leq \pi \qquad \text{Eq 3}$$

$$sin2\chi = \frac{2E_{0x}E_{0y}}{{E_{0x}}^2 + {E_{0y}}^2} sin\delta, -\pi/4 < \chi \leq \pi/4 \qquad \text{Eq 4}$$

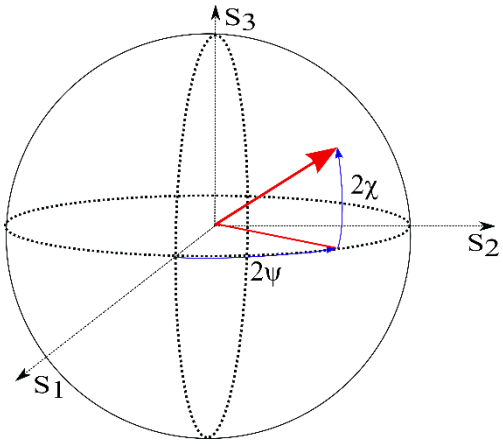

Figure 2.3 : A representative Poincare ellipse

The equations 3 and 4 describe the polarization state of light and are a very good representation system. However, the elliptical representation has a primary drawback that if passed through multiple polarizing media, the calculation becomes extremely tedious and very difficult to visualize the relative change in the polarization state of light. As a result, a spherical representation of polarization states of light was introduced known as Poincare sphere (Fig 2.3). The parametrization of Poincare sphere and its relation to the polarization ellipse parameters is shown in equation 5[49].

Parametrization of the sphere:

$$x = cos(2\chi) \cdot cos(2\psi) \qquad \text{Eq 5a}$$

$$y = cos(2\chi) \cdot sin(2\psi) \qquad \text{Eq 5b}$$

$$z = sin(2\chi) \qquad \text{Eq5c}$$

$$x^2 + y^2 + z^2 = 1 \qquad \text{Eq 5d}$$

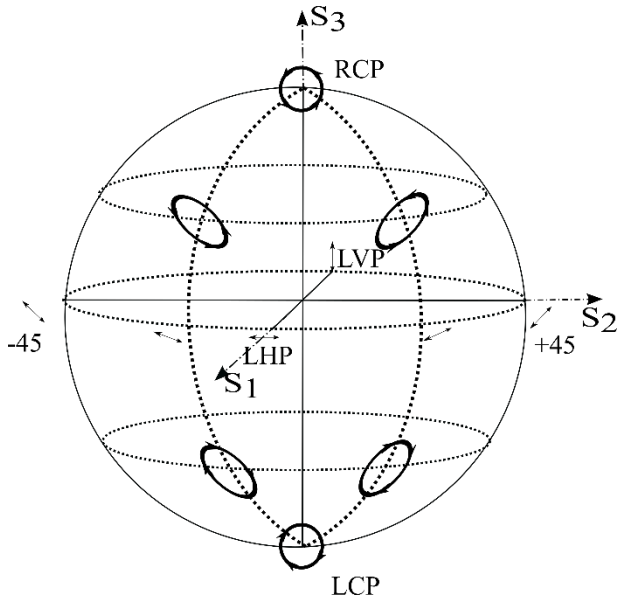

Figure 2.4 : Different polarization states of light on a Poincare sphere along with degenerate states of light

The χ and ψ in Figure 2.4 can be related to the polarization ellipse. Since, χ and ψ were the characteristic properties of the polarization ellipse and polarization state of light, each of the point on the surface of Poincare sphere represents a unique polarization state of light and corresponding polarization ellipse. Figure 2.4 shows the different polarization ellipses corresponding to the regions along with the degenerate states of light. We can observe from the ellipse that if a point is on the equator of Poincare sphere, light is linearly polarized. The polarization state of light will have a right-handed rotation in the top hemisphere and left-handed in the bottom hemisphere of the Poincare representation. The poles represent the circularly polarized light and each of the point on the surface outside of the equator and poles is a configuration of elliptically polarized light.

2.2 Stokes parameters

The Poincare sphere representation gives us an avenue of analysis of multiple polarization states represented on a single graph and being able to analyze the respective images. However, each point on the sphere is also an instantaneous representation of polarization state of the light. The instantaneous representations are not the direct measurable quantities for the polarization state of light. The measurable quantities for polarization state of light can be obtained by time averaging the polarization ellipse as shown in equation 6 to obtain equation set 7[49,50].

$$< E_i(z,t), E_j(z,t) > = \lim_{T\to\infty} \frac{1}{T} \int_0^T E_i(z,t) E_j(z,t) dt, \qquad i,j = x,y \qquad \text{Eq 6}$$

$$S_1{}^2 = S_2{}^2 + S_3{}^2 + S_4{}^2 \qquad \text{Eq 7a}$$

$$S_1 = E_{0x}{}^2 + E_{0y}{}^2 \qquad \text{Eq 7b}$$

$$S_2 = E_{0x}{}^2 - E_{0y}{}^2 \qquad \text{Eq 7c}$$

$$S_3 = 2E_{0x} \cdot E_{0y} \cdot cos\delta \qquad \text{Eq 7d}$$

$$S_4 = 2E_{0x} \cdot E_{0y} \cdot sin\delta, \delta = \delta_y - \delta_x \qquad \text{Eq 7e}$$

The matrix representation of equation set 7 can be seen below:

$$\begin{pmatrix} I \\ Q \\ U \\ V \end{pmatrix} = \begin{pmatrix} S_1 \\ S_2 \\ S_3 \\ S_4 \end{pmatrix} = \begin{pmatrix} {E_{0x}}^2 + {E_{0y}}^2 \\ {E_{0x}}^2 - {E_{0y}}^2 \\ 2E_{0x} \cdot E_{0y} \cdot cos\delta \\ 2E_{0x} \cdot E_{0y} \cdot sin\delta \end{pmatrix}$$

$$S_{LHP} = I_0 \cdot \begin{pmatrix} 1 \\ 1 \\ 0 \\ 0 \end{pmatrix}, S_{LVP} = I_0 \cdot \begin{pmatrix} 1 \\ -1 \\ 0 \\ 0 \end{pmatrix}, S_{L+45P} = I_0 \cdot \begin{pmatrix} 1 \\ 0 \\ 1 \\ 0 \end{pmatrix}, S_{L-45P} = I_0 \cdot \begin{pmatrix} 1 \\ 0 \\ -1 \\ 0 \end{pmatrix},$$

$$S_{RCP} = I_0 \cdot \begin{pmatrix} 1 \\ 0 \\ 0 \\ 1 \end{pmatrix}, S_{LCP} = I_0 \cdot \begin{pmatrix} 1 \\ 0 \\ 0 \\ -1 \end{pmatrix}$$

The Stokes parameter S_1 or I represent the total intensity of the beam. The S_2 or Q represents the preponderance of LHP over LVP. The S_3 or U represents the preponderance of L+45P over L-45P and S_4 or V represents the preponderance of RCP over LCP. These can be found experimentally by varying the angle between a waveplate and polarizer in a classical Stokes measurement set up where the light is passed through a waveplate and a linear polarizer described in the following sections.

2.3 Mueller calculus:

If there is an input beam with characteristic polarization state of 4X1 matrix and there is an output light beam with a different characteristic polarization state with 4X1 matrix there exists a 4X4 transformation matrix relating the material properties of matter to the optical behavior of interacting light. This transformation matrix for Stokes parameter calculations is known as the Mueller matrix[51] and is described in equation 8.

$$S_{out} = M.S_{in} \qquad \text{Eq 8}$$

$$\begin{pmatrix} S_1^{out} \\ S_2^{out} \\ S_3^{out} \\ S_4^{out} \end{pmatrix} = \begin{pmatrix} m_{00} & m_{01} & m_{02} & m_{03} \\ m_{10} & m_{11} & m_{12} & m_{13} \\ m_{20} & m_{21} & m_{22} & m_{23} \\ m_{30} & m_{31} & m_{32} & m_{33} \end{pmatrix} . \begin{pmatrix} S_1 \\ S_2 \\ S_3 \\ S_4 \end{pmatrix}$$

Based on the phenomenological interaction between light and matter, Mueller matrix can be further decomposed into various components to represent phenomenon of birefringence, diattenuation, rotation and refraction.[40][48]

2.4 Jones calculus:

An alternative calculus representation of the Mueller calculus is the Jones calculus. The Jones calculus introduces Jones vectors which contain the complex electric field components of light shown in the matrix representation below.

$$\boldsymbol{E} = \begin{pmatrix} E_x \\ E_y \end{pmatrix} = \begin{pmatrix} E_{0_x}^{i\delta_x} \\ E_{0_y}^{i\delta_y} \end{pmatrix}$$

Similar to the Mueller calculus, the Jones matrix is the transformation matrix that will describe the polarization event in the light matter interaction.

$$\mathrm{E}^{\mathrm{out}} = \mathrm{J}.\mathrm{E}^{\mathrm{in}} \qquad \text{Eq 9}$$

$$J = \begin{pmatrix} j_{xx} & j_{xy} \\ j_{yx} & j_{yy} \end{pmatrix}$$

The Jones calculus is simpler compared to Mueller calculus because it has one less degree of freedom compared to Mueller matrix.[52] As a result partial polarization state interactions cannot be calculated using Jones calculus.[49]

2.5 Classification of optically active matter:

The mathematical characterization from the light perspective and the change in the polarization state can be used to characterize the anisotropy of matter. The material that can cause a change in the polarization state of light by virtue of its anisotropy is called as optically active material. The characteristic properties of optically active matter are birefringence and dichroism.

Birefringence: Birefringence is the property of a material to refract an incident light into two different components based on the difference in the propagation speeds due to the anisotropy along and orthogonal to the optical axis.[53] The birefringence can be classified into circular and linear birefringence. The circularly birefringent material, also known as gyro tropic material[54], can change the degree of circular polarization state of light between RCP and LCP causing a change in the phase of the polarization state resulting in rotation. This effect can be observed in chiral media or optically active metamaterials.[55],[56] The linear birefringence is the ability of a material to similarly divide the material beam into two linearly polarized beams with different linear polarized states.[57] Crystals like Calcite, Quartz most polymers exhibit linear birefringence.

Dichroism is the property of optically active material to differentially absorb the polarization components of light. Similar to birefringence, Dichroism can also be classified as either linear or circular dichroism. Circular dichroism is the difference in absorption of LCP and RCP light with respect to the optical center.[58] Circular dichroism is the principle used for CD

spectroscopy where the structure of chiral molecules can be determined. Linear dichroism or diattenuation is the difference between the absorption of polarized light along and orthogonal to the optical axis.[58]

2.6 Polarimetry

2.6.1 Stokes polarimetry

As discussed earlier, the polarization are the measurables for the polarization state of light. The polarization states of light can only be measured relative to each other as described in equations 6 and 7. The optical configurations relating to the equations are shown in Figure 2.5 [50,59].

The experimental setup for the Stokes polarimetry tries to emulate these configurations. There are different methods like liquid crystal variable retarder[60–62], Plasmonic

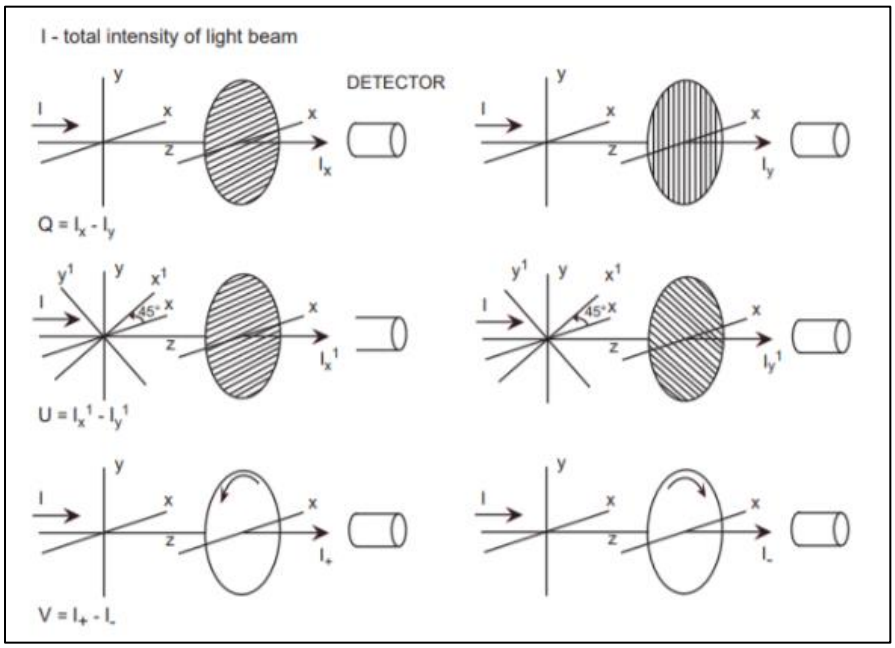

Figure 2.5[59]: Experimental configuration for stokes polarimetry

nanomaterial-based polarimetry[63–65] or a simple combination of waveplate and polarizer configurations to achieve configurations shown in Figure 2.5.

2.6.2 Mueller matrix polarimetry

Similar to the Stokes polarimetry, Mueller matrix polarimetry can be achieved using 2 sets of quarter waveplate and polarizer setup (Fig 2.6B). The first set is a series of a quarter waveplate and a polarizer that will act as polarization state generator or PSG (Fig 2.6 A). The second set is the polarization state analyzer or PSA. In a single experimental measurement, 9 of 16 parameters can be obtained if the PSG can deconvolute each of the frequencies using a complex system of photo elastic modulators and lock in amplifiers.[43] In a more accessible configuration, for a full Mueller matrix measurement there need to be taken 36 measurements as shown by He et. a1 (2013) in equation 10. [41]

Eq 10

$$\begin{pmatrix} m_{00} & m_{01} & m_{02} & m_{03} \\ m_{10} & m_{11} & m_{12} & m_{13} \\ m_{20} & m_{21} & m_{22} & m_{23} \\ m_{30} & m_{31} & m_{32} & m_{33} \end{pmatrix}$$

$$= 0.5 \begin{pmatrix} \mathrm{HH} + \mathrm{HV} + \mathrm{VH} + \mathrm{VV} & \mathrm{HH} + \mathrm{HV} - \mathrm{VH} - \mathrm{VV} & \mathrm{HH} + \mathrm{HV} + \mathrm{VH} + \mathrm{VV} & \mathrm{HH} + \mathrm{HV} + \mathrm{VH} + \mathrm{VV} \\ \mathrm{HH} - \mathrm{HV} + \mathrm{VH} - \mathrm{VV} & \mathrm{HH} - \mathrm{HV} - \mathrm{VH} + \mathrm{VV} & \mathrm{PH} - \mathrm{PV} - \mathrm{MH} + \mathrm{MV} & \mathrm{RH} - \mathrm{RV} - \mathrm{LH} + \mathrm{LV} \\ \mathrm{HP} + \mathrm{HM} + \mathrm{VP} + \mathrm{VM} & \mathrm{HP} - \mathrm{HM} - \mathrm{VP} + \mathrm{VM} & \mathrm{PP} - \mathrm{PM} - \mathrm{MP} + \mathrm{MM} & \mathrm{RP} - \mathrm{RM} - \mathrm{LP} + \mathrm{LM} \\ \mathrm{HR} - \mathrm{LL} + \mathrm{VR} - \mathrm{RL} & \mathrm{HR} - \mathrm{VR} + \mathrm{VL} - \mathrm{HL} & \mathrm{PR} - \mathrm{MR} + \mathrm{ML} - \mathrm{PL} & \mathrm{RR} - \mathrm{RL} - \mathrm{LR} + \mathrm{LL} \end{pmatrix}$$

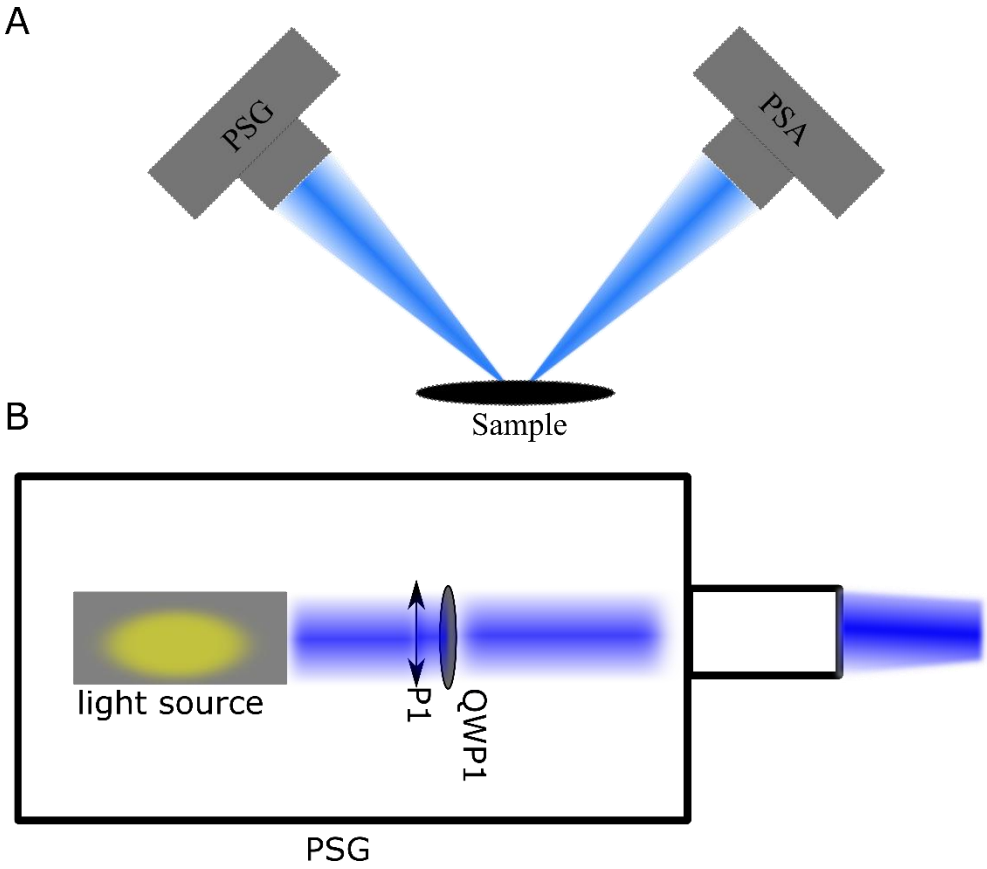

Figure 2.6: A) Mueller matrix polarimetry setup with polarization state generator (PSG) and polarization state analyzer (PSA). B) Schematic of polarization state generator (PSG)

For equation 10, each of the parameter in the element has a specific incoming light configuration and outgoing configuration. Each of the incoming configuration is a degenerate state generated by PSG. The parameters are related to the polarizer position relative to the degenerate states of light i.e., H for LHP, V for LVP, P for +45P, M for -45P, L for LCP and R for RCP. For example, HH means the image obtained by having the incoming polarization configuration for LHP and outgoing for LHP as well.

2.7 Section 2 acknowledgement

Section 2, in part has been submitted for submission for publications of the materials as it may appear in *Advanced Optical Materials*, 2021, Eric S. A. Goerlitzer; Aniket S Puri; Jebin J. Moses; Lisa V. Poulikakos; Nicolas Vogel.

3. Characterization techniques

3.1 Microscopy

The polarized light microscopy (PLM) was carried out as optical characterization technique.

In PLM a quarter wave plate and linear polarizer are the optical elements from the microscope used for manipulation of the polarization state of light. The quarter wave plate (Nikon P-CL λ/4 @540 nm) is an element that introduces a quarter of a wavelength retardance along the axis of the transmitting light. The primary function of a quarter wave plate from the perspective of the experiments is to convert linearly polarized light to circularly polarized light. This can be calculated from equation 8 where, M = M_{qwp} (Mueller matrix of quarter wave plate at 45^0 to linear axis: equation 11) S_{in} = incoming linearly polarized light and S_{out} = resultant circularly polarized light.

$$M_{qwp} = 1/2\begin{pmatrix} 1 & 0 & 0 & 0 \\ 0 & 1 & 0 & 0 \\ 0 & 0 & 0 & -1 \\ 0 & 0 & -1 & 0 \end{pmatrix} \qquad \text{Eq 11}$$

For the microscopy setup, the linear polarizer (Nikon D-DP rotatable polarizer) is the second important component that is used for obtaining the linearly polarized degenerate states of light. The equation for the linear polarizers used is shown in the matrix below where M_{lp} is the linear polarizer Mueller matrix, and γ is the angle between the x and y components of amplitude attenuation. Similar to the calculations performed for the quarter wave plate, the outgoing polarization can be obtained by using equation 8 where M = M_{lp} and the Mueller matrix of the linear polarizer is shown in equation 12.

$$Mlp = 1/2\begin{pmatrix} 1 & cos(2\gamma) & 0 & 0 \\ cos(2\gamma) & 1 & 0 & 0 \\ 0 & 0 & 0 & sin(2\gamma) \\ 0 & 0 & sin(2\gamma) & 0 \end{pmatrix} \quad \text{Eq 12}$$

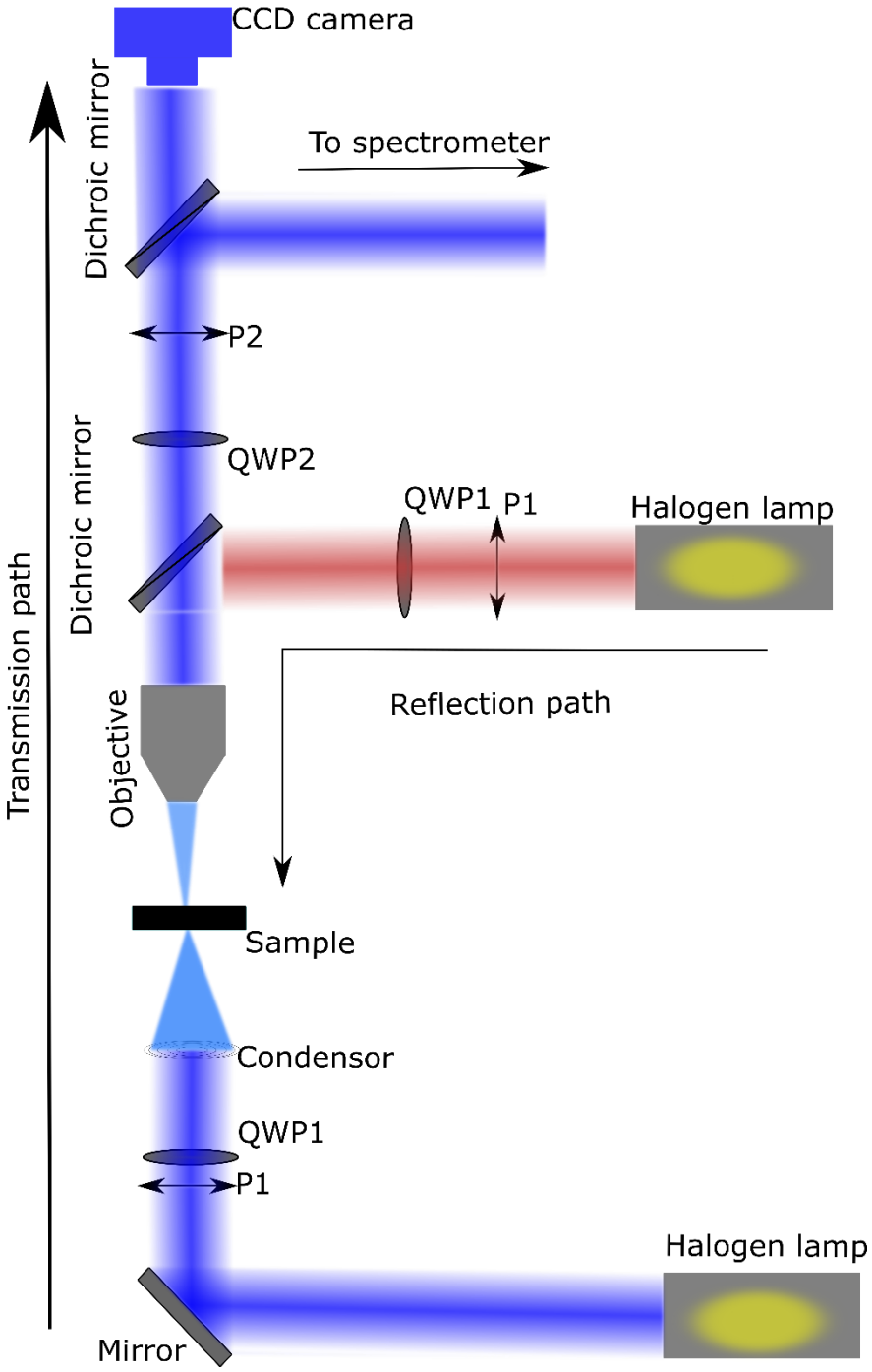

Figure 3.1: Optical path for Nikon LV100 ND microscope

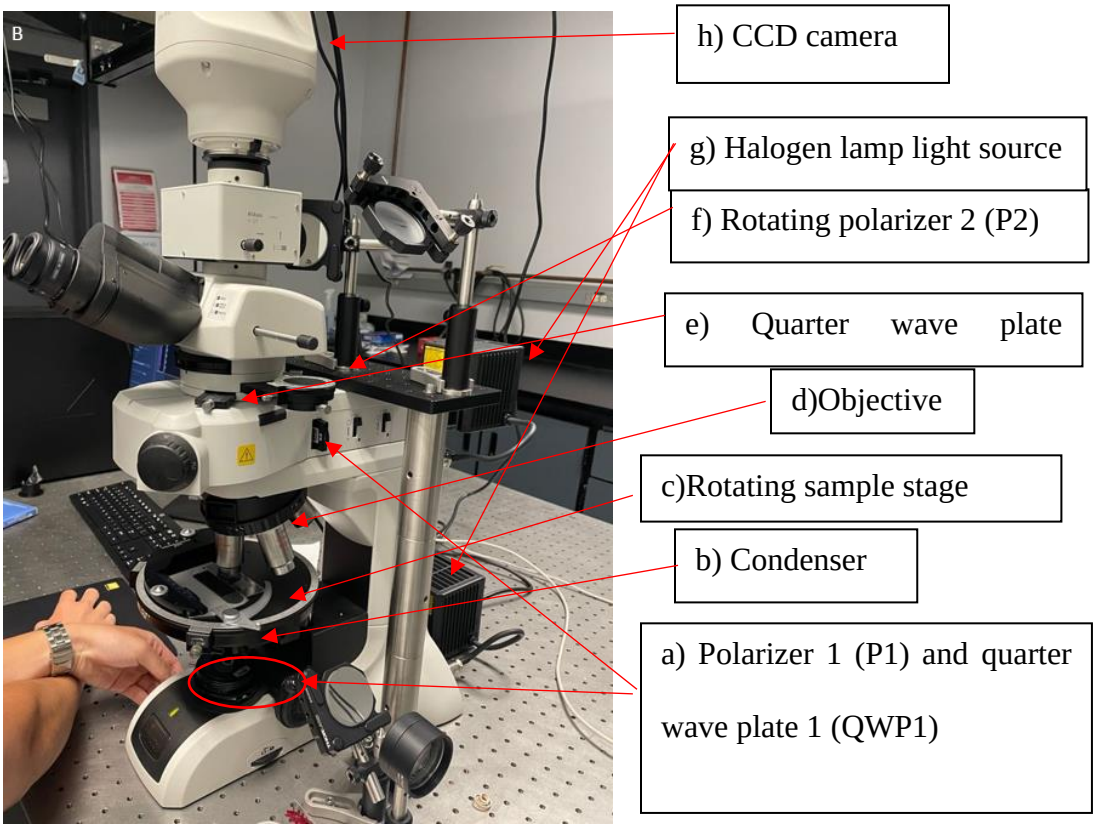

Figure 3.2 The Nikon LV 100 ND microscope

The LV 100 ND uses halogen lamps for illuminations of the sample. These can be seen in the cage depicted by ‘g’ in Figure 3.2. The upper lamp and lower lamps are for illumination in reflectance and transmission mode respectively (Fig 3.1 and 3.2). In both the reflectance and transmission mode, the aperture can be adjusted by using the knob in the light path. For the experiments performed here we used the aperture to vary the region of interest experimentally for an average intensity measurement. The region of interest can also be defined using the NIS elements software and the subsequent analysis can be carried out as well. The component ‘a’ shown in Figure 3.2 is a combination of quarter wave plate and polarizer in transmission mode and reflectance mode in the respective paths. These can be useful for Mueller matrix polarimetry and act as PSA for the measurements (Fig 2.6). The component ‘c’ is a rotating stage where the sample

is excited with the light. The microscope has 4 different objectives (TU Flour Nikon objectives) at component ‘d’ with adjustable 5X, 10X, 20X, 50X and 100X optical zoom. The component ‘e’ is the retractable quarter wave plate. The component ‘f’ is a retractable rotating linear polarizer (P2) used for filtering the polarization of light along the outgoing light path. The component ‘h’ is the CCD camera (Nikon DS-Ri2) used for microscopy images. The camera can be operated in three different modes namely, bino, photo and spectroscopy by adjusting the dichroic mirror path shown in Figure 3.1.

Using configuration from Figure 2.5 and the optical light path shown in Figure 3.1 A, we can obtain Stokes’s polarimetry images. 7 images need to be obtained in accordance with the configurations that are described in table 3.1 for obtaining the full Stokes polarimetry.

Table 3.1 : Images obtained for measurement of Stokes parameters

Image	Polarizer 1	Quarter wave plate	Stokes configuration
Image 1	Not inserted	Not inserted	I
Image 2	Inserted at 0	Not inserted	I0
Image 3	Inserted at 45	Not inserted	I45
Image 4	Inserted at 90	Not inserted	I90
Image 5	Inserted at 135	Not inserted	I135
Image 6	Inserted at 0	Inserted	RCP
Image 7	Inserted at 90	Inserted	LCP

Following the imaging of the degenerate state of light for each of the sample described in above table, the individual Stokes parameters Q, U, V can be obtained as described in Figure 2.5. The I, Q, U, V for each sample are obtained by using the MATLAB code (refer appendix 6.2.1).

After obtaining the I, Q, U, V the next step is to define the degree of polarization parameters. The three parameters defined for this set of experiments are degree of linear polarization (DOLP), Degree of circular polarization (DCP) and degree of polarization (DOP). The DOLP, DCP and DOP are calculated according to the equation 13a, 13b, 13c respectively.[66,67]

$$DOLP = \frac{\sqrt{Q^2 + U^2}}{I} \qquad \text{Eq 13a}$$

$$DCP = \frac{|V|}{I} \qquad \text{Eq 13b}$$

$$DOP = \frac{\sqrt{Q^2 + U^2 + V^2}}{I} \qquad \text{Eq 13c}$$

4. Polarized light microscopy analysis

4.1 Collagen

4.1.1 Materials and methods

Rat tail type 1 collagen was obtained from Fischer scientific (C3087) for the experimentation. The initial concentration of collagen was 4-5mg/ml. For the experiments, the pH and temperature were chosen as parameters of choice to be varied. The pH was varied as 7, 8, 9, 10. The ionic strength was kept at 0.4. The collagen was maintained at 4 ^{0}C. The collagen pH was varied on ice using the Eppendorf frozen in ice (see Fig 4.2). The collagen gelling was carried out at room temperature (22 ^{0}C) and at 40 ^{0}C on a magnetic hot plate. The pH was measured by pipetting out 5 microliters onto a pH paper of mixture for every pH adjustment.

A constant 300 microliters of collagen were pipetted into a 3 ml Eppendorf. Following which acetic acid was titrated to a pH of 3. The solution was titrated with Sodium hydroxide (NaOH) as base and Sodium bicarbonate ($NaHCO_{3)}$ as a buffer for obtaining the required pH. Finally, 10 % v/v of the final volume Phosphate buffered saline (PBS) was added to the collagen

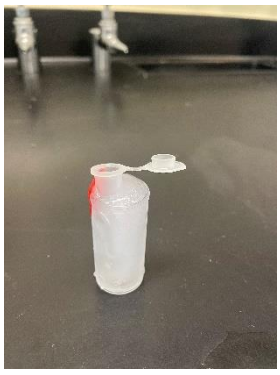

Figure 4.1: Eppendorf frozen in ice for collagen experiments

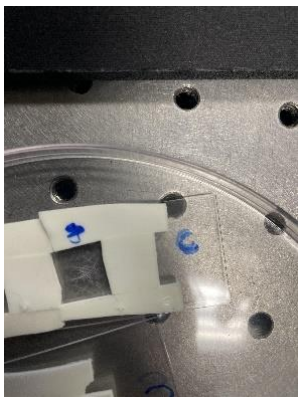

Figure 4.2: Custom prepared wells for collagen polymerization

solution. The collagen was then pipetted onto the petri dish or the custom prepared wells that are shown in Figure 4.2 for polymerization. The collagen synthesis was conducted on ice, using the frozen Eppendorf shown in Figure 4.1.

The collagen samples were subsequently imaged on a polarized light microscope for analysis.

4.1.2 Results and Discussions

For the first set of collagen imaging, 450 microliters of collagen mixture were pipetted onto a 26 mm diameter culture plate.

The resulting images is shown in Figure 4.3. This image is an optical microscopy image where the sample is excited by a linearly polarized light oriented in 0 to 90^0 orientation. In the overall area of the well plate, the polymerization of collagen was found to be very sparse. We found very few strands of polymerized fibrillar collagen in this image set. On the periphery particles dispersed (highlighted in red) throughout the plate can be observed. These are a combination of sparsely polymerized collagen and possibly the particulate artefacts on the glass slide. Changing the polarizer orientation in the outgoing path in the microscope did not give any

Figure 4.3: Image of collagen synthesized at 9 pH and room temperature in a 26 cm diameter well plate at 10X magnification. Scale = 100 μm

appreciable information during this particular imaging. However, this experimentation was the first confirmation of collagen being polymerized and forming fibrils. Subsequently, collagen was prepared in custom wells (Fig 4.2) to restrict the volume and increase the molecular crowding of collagen for synthesis.

Custom well polymerized collagen provided information on microstructural analysis of collagen (Fig 4.4 and .4.5). More fibrillar features can be observed in both Figure 4.4 and 4.5. The images here were obtained as a reference image of no polarizer in the outgoing path for microscopy (Fig 4.5) and a cross polarized image where axis of polarizer P2 along the outgoing path is orthogonal to the incoming polarizing light (Fig 4.5). The Figure 4.5 image shows that the visualization of collagen microstructural features is enhanced when the polarizers are cross polarized (P1 and P2 in Figure 3.1 are orthogonal to each other). The ability to see the microstructural features of collagen organization in images obtained during cross polarization of polarizers is due to the optical anisotropy of the collagen fibers.

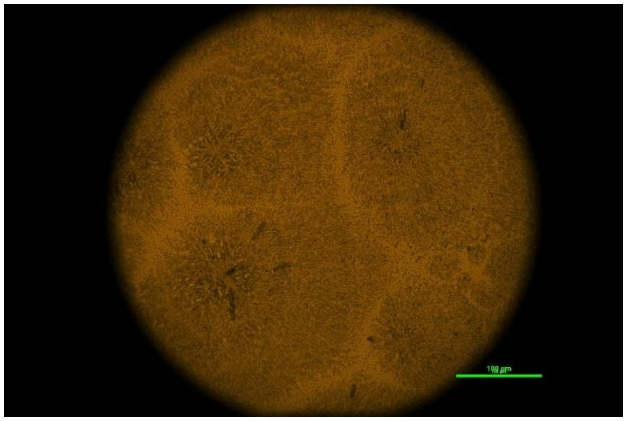

Figure 4.4: Collagen image without P2 at 8 pH and 40^0C and 20 X magnification Scale = 100 μm

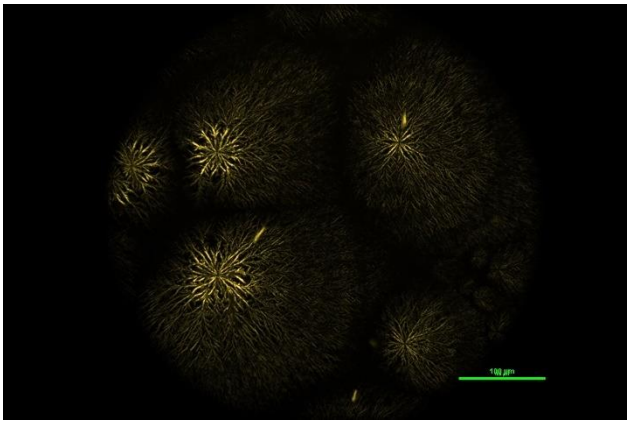

Figure 4.5 : Cross polarized collagen image at 8 pH and 40^0C and 20 X magnification. Scale = 100 μm

Comparing Figure 4.5 and 4.7, we can see that the collagen at room temperature has a more sheet like appearance as compared to the branching at 40 ^{0}C temperature. The comparison of Figure 4.5 and 4.7 shows the effect of faster kinetics in collagen polymerization.[68–70] For collagen synthesized at room temperature, there appear to be dark spots of accumulations (highlighted by red circles in image 4.6) of collagen throughout the image of the polymerized collagen matrix. In image 4.6 we can see that these dark spots have a distinctive pattern of Maltese cross structures. The Maltese cross structures provide information about the structure of the biomaterial[71]. The corresponding images show that only the Maltese cross structures are birefringent in case of

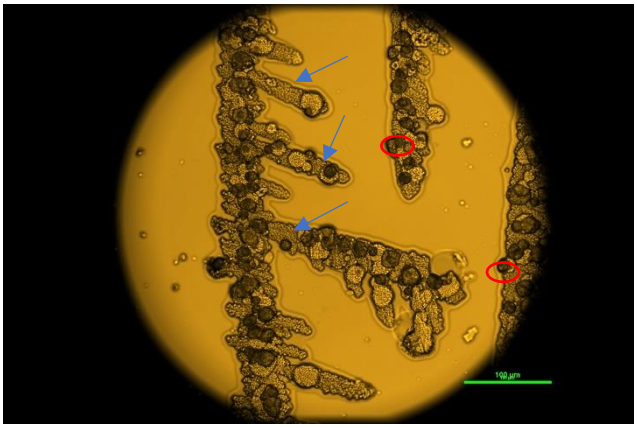

Figure 4.6 : Collagen image without polarizer P2 at room temperature and 8pH Scale = 100 μm

Figure 4.7: Collagen image with cross polarizers at room temperature and 8 pH Scale = 100 μm (image enhanced for visibility from Appendix Figure 6.1)

collagen polymerization, because the polymerized parts that do have more sheet like structures (pointing arrows in Fig 4.6) do not appear in the cross polarized image. In assessing the polymeric properties of starch, it is shown that light microscopy can prove to be an even more powerful tool than scanning electron microscopy in reference to samples with Maltese cross structures. [72–74]. The Maltese cross structures have shown to be a consequence of lamellar folding of polymers on each other in case of Elastin like recombinant materials and other spherulite forming polymeric structures.[71,75] The formation of Maltese cross structures is a consequence of different

crystalline phases for starch, protein and fat materials.[35–37] The Maltese cross structures indicate a possible crystalline phase formed in the synthesized collagen matrices.

Following the above observations, we conducted a stage rotation study using polarized light microscopy. From movie S1 (Puri_01_rotation_S1) for collagen synthesized at room temperature and pH 8, It can be seen that the orientation of the cross pattern does not change during rotation of the stage. Similarly, for the pH 8 at temperature of 40 ^{0}C in movie S2 (Puri_01_rotation_S1), a very small cross pattern at the center can be observed that behaves in a similar way. These observations show credence to the theory that similar to spherulitic crystal formation, collagen follows a nucleation and growth mechanism [76,77] The observations support a claim that there is formation of crystallite patterns at the center as evidenced by their Maltese cross structural appearance. These patterns then grow and form collagen fibrils as the molecular entanglement increases due to faster kinetics at higher temperature. The results of the faster kinetics can be seen in Figure 4.4 where the collagen branches seem to have grown from the center. The movie S2 (Puri_02_rotation_S2) of the collagen synthesized at 40 ^{0}C, show that there are regions of collagen on periphery that change the illumination and reappear and disappear as the sample is rotated. Near the center of each of the collagen cluster, we can see that there are not as many fluctuations. Since the outgoing light behavior shows a dependence on the polarization state of excited light, we can conclude that the collagen fibrils are birefringent in nature and more anisotropic compared to the collagen synthesized at lower temperature due to the brightness of each of the patterns. Some fibers exhibit birefringence, but there also are several regions that might show other optical anisotropic properties. Most fibrous materials will show birefringence due to the alignment of the molecules along the orientation of the fiber. However, the bulk polymers will not show as strong a birefringence effect because of the random orientation of the material.[78]

We can see this effect in the behavior of collagen for cross polarized and unpolarized image samples.

For further characterization of the optical properties of the collagen, a Stokes parameter measurement was conducted according to the protocol shown in chapter 3 using the MATLAB code described in appendix (6.2.1). The Stokes parameters images are measuring the outgoing polarization state of light. The purpose of the imaging experiment here is to see if the outgoing light provides insight onto the structural properties of collagen.

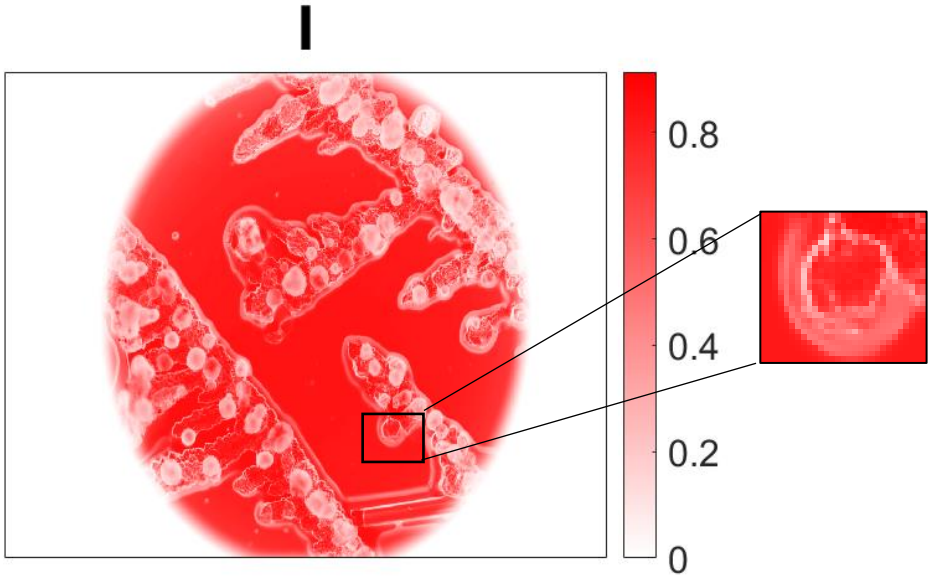

Figure 4.8 First Stokes parameter (I) for collagen synthesized at 8 pH and room temperature. Inset highlighting region of Maltese cross structure.

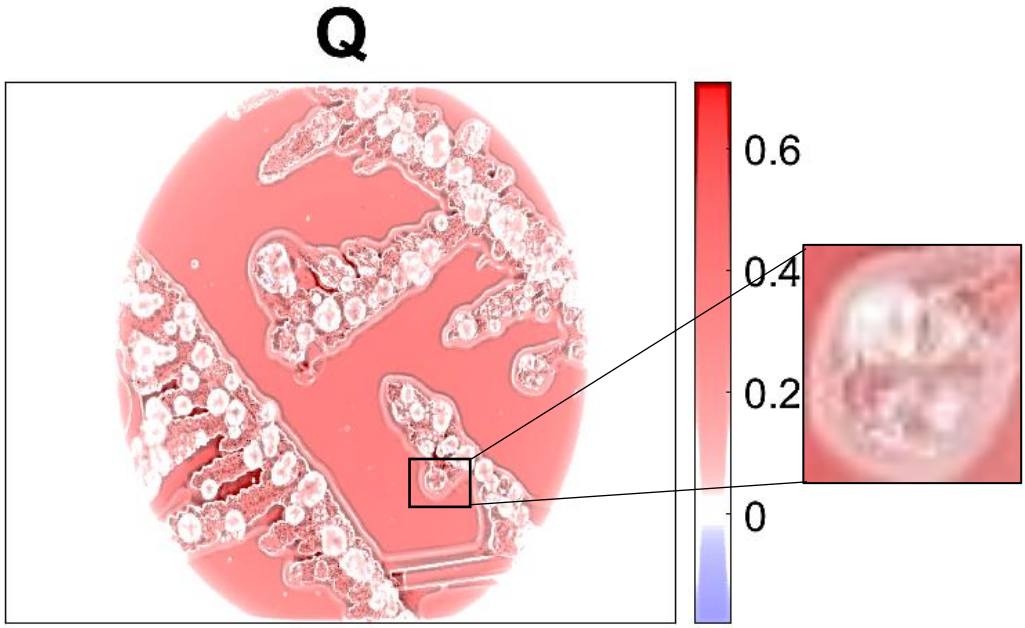

Figure 4.9 : Second Stokes parameter (Q) image for collagen synthesized at 8pH and room temperature. Inset highlighting region of Maltese cross structure (image enhanced for visibility from Appendix Figure 6.3)

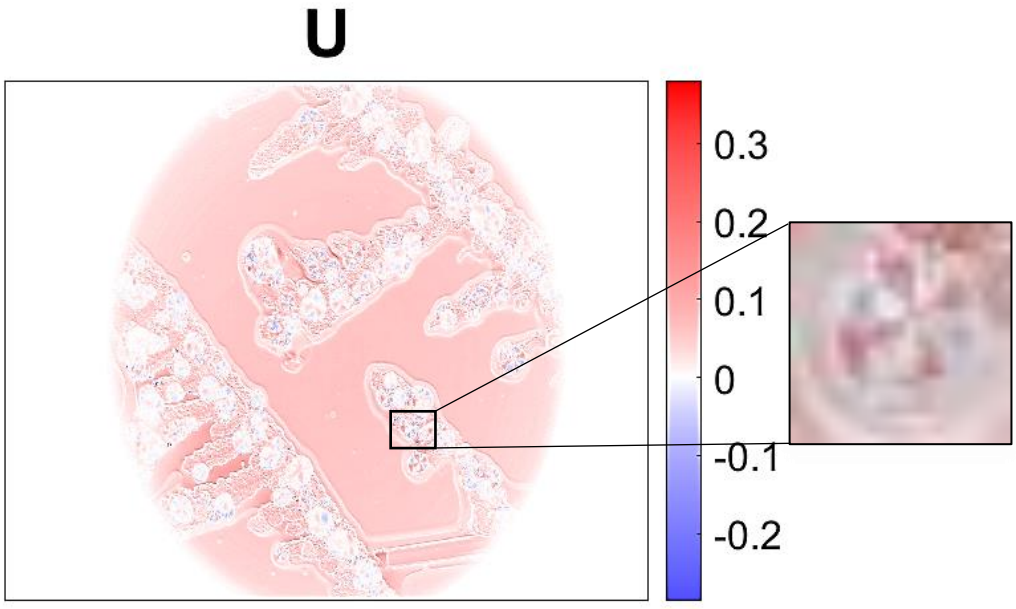

Figure 4.10: Third Stokes (U) parameter image for collagen synthesized at 8 pH and room temperature Inset highlighting region of Maltese cross structure (image enhanced for visibility from Appendix Figure 6.2)

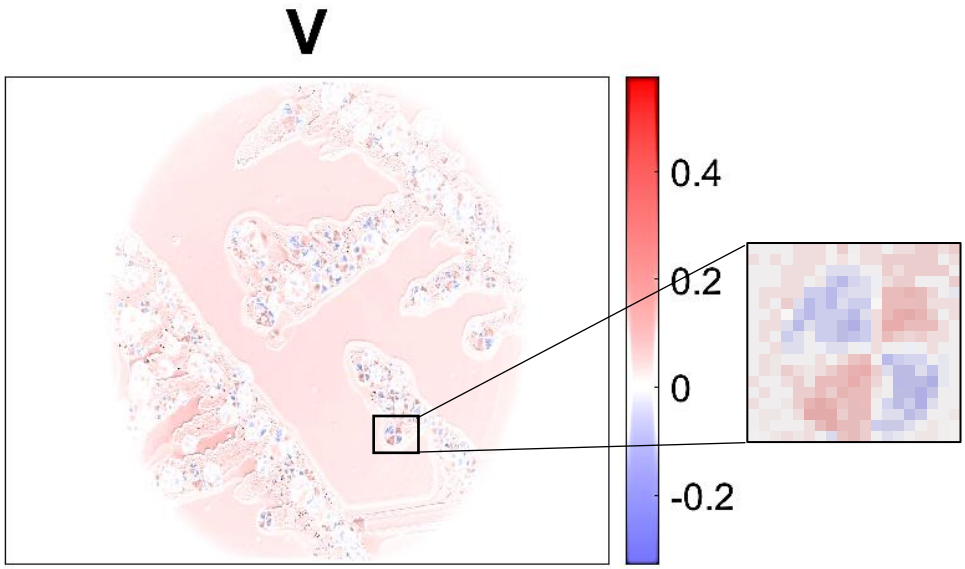

Figure 4.11 : Fourth Stokes parameter (V) image of collagen synthesized at room temperature and 8 pH. Inset highlighting region of Maltese cross structure (image enhanced for visibility from Appendix Figure 6.4)

An important consideration for all of the Stokes parameter is the polarization state of light excited light. Since the sample is excited by linearly polarized light whose polarization is oriented in 0^0 - 90^0 angle, the maximum background light will transmit through in case of the first and second Stokes parameter measurements. This phenomenon can be observed from the higher brightness of the background and sample observed in Figure 4.8 and 4.9. Similarly, since the incoming light is not oriented at 45^0 and has no circular polarization state, the Figure 4.10 and 4.11 appear to have lower intensity values. A closer look at the cross inset regions on each of the Figures from 4.8 to 4.11, shows that except for the first Stokes parameter, every one of them shows a Maltese cross pattern. The appearance of Maltese cross patterns in these images reinforces the idea that the optical activity of collagen plays an important role in polarized light microscopy. The pattern is not as distinct comparatively for the first Stokes parameter because of the background

light being polarized parallel to the parameter Q axis i.e., 0^0-90^0. An observation that can be made for the Maltese crosses for each of the material is that the direction of the cross for second Stokes parameter (Figure 4.9 - inset cross) is complementary to that of the third Stokes parameter (Figure 4.10 - inset cross). For reference, the inset cross in Figure 4.9 with high intensity values (~0.2-0.4) is vertically aligned. However, the inset cross with high intensity values (~0.2-0.6) in figure 4.10 is at an angle approximately 30^0 rotated counterclockwise to the vertical alignment. These observations further provide justification for the hypothesis that the structure of the material consist of semicrystalline lamellar sheets oriented radially as described in Elsharkawy et. al (2018) due to the pseudo isotropic behavior of polarization state of light.[79] In Figure 4.11 (inset), the fourth Stokes parameters show the cross structure with 2 radially outward arms as opposed to 4 in case of the second (Figure 4.9 inset) and third Stokes (Figure 4.10 inset) parameter. This indicates that these Maltese cross structures exhibit a different retardance for circular polarization and linear polarization states. This could also be a result of additional interference due to the diattenuation and optical activity of the material.

As a consolidation of all of the data, the overall degree of polarization parameters was calculated as shown in the Figures 4.8 to 4.11 in accordance with the equations 13a to 13c.

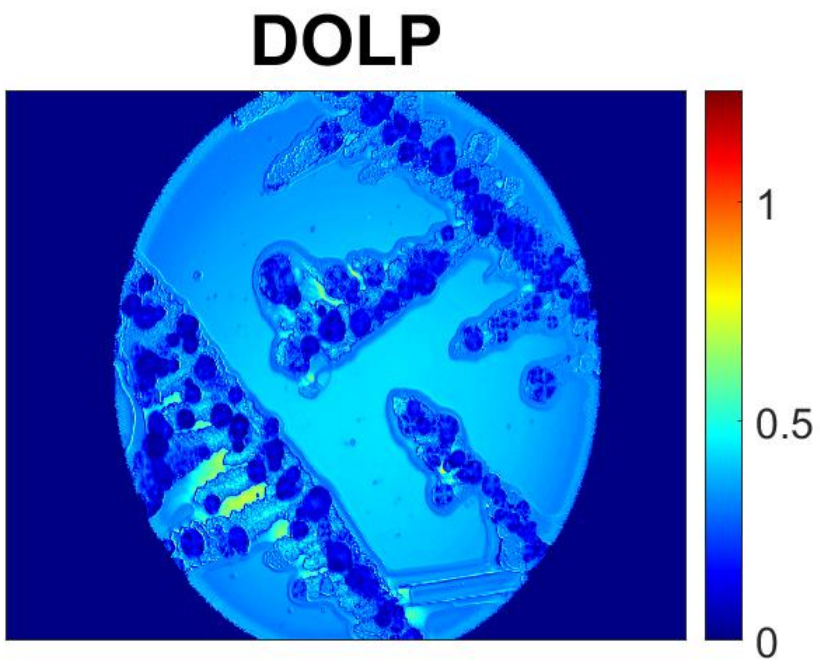

Figure 4.12 : DOLP image of collagen synthesized at room temperature and 8 pH

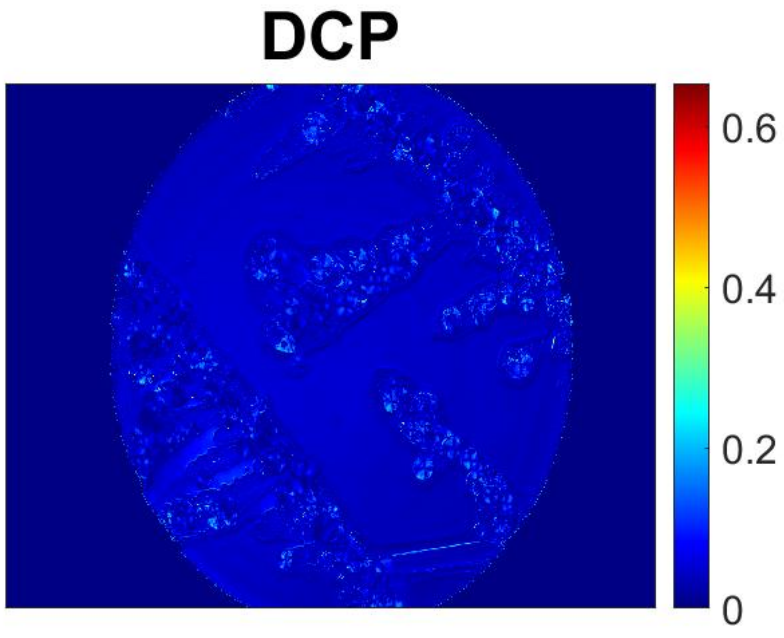

Figure 4.13 : DCP image of collagen synthesized at room temperature and 8 pH

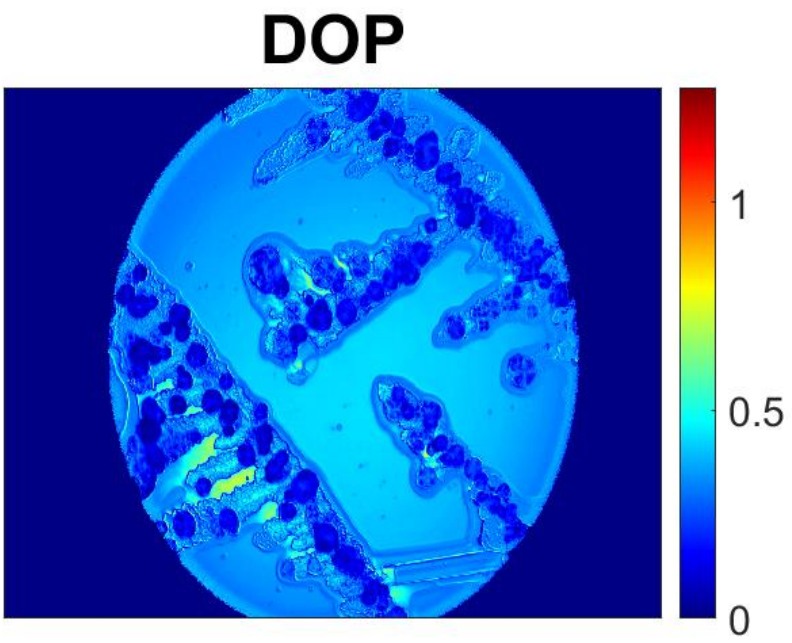

Figure 4.14 : DOP image of collagen synthesized at room temperature and 8 pH

From the above Figures, DOLP (Figure 4.12) shows the regions of no sample to have the brightest values (>0.4). This is expected due to the linearly polarized background signal. Similarly, the DOLP is represented dominantly in the overall DOP image. In previous research conducted by Shi et. al. (2021), starch was found to show Maltese cross structures similar to the structures shown here as a consequence of birefringence.[75] Further investigation needs to be conducted to understand the role of structure and crystallinity in the formation of the Maltese cross structures and the exact effects leading up to the nature of birefringence caused.

Following the room temperature collagen imaging, the Stokes parameters for the collagen synthesized at higher temperature of 40 ^{0}C were subsequently analyzed.

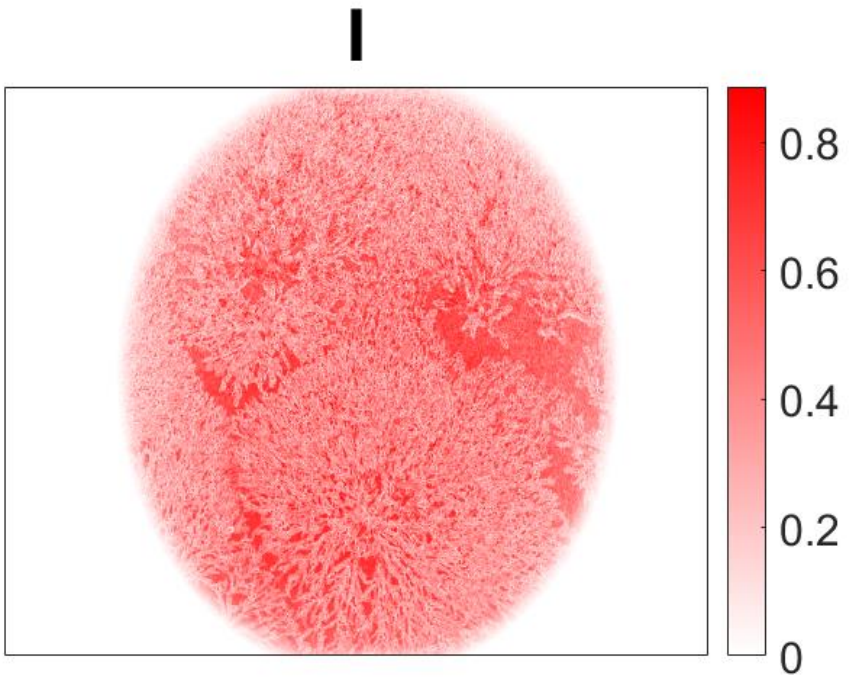

Figure 4.15 : Stokes parameter I image for collagen synthesized at 40 ^{0} C and 9 pH

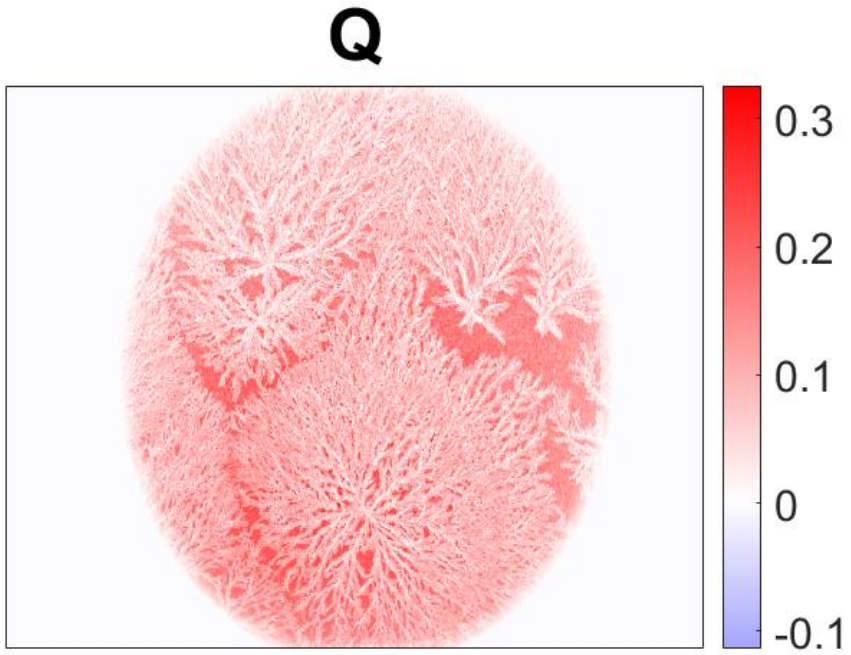

Figure 4.16 : Stokes parameter Q image of collagen synthesized at 40 ^{0} C and 9 pH

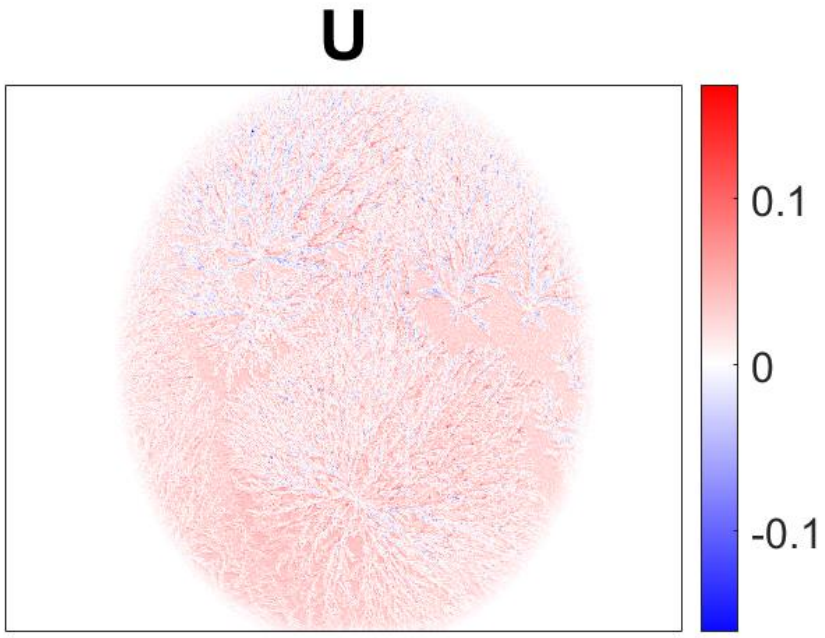

Figure 4.17 : Stokes parameter U image of collagen synthesized at 40 ^{0} C and 9 pH.

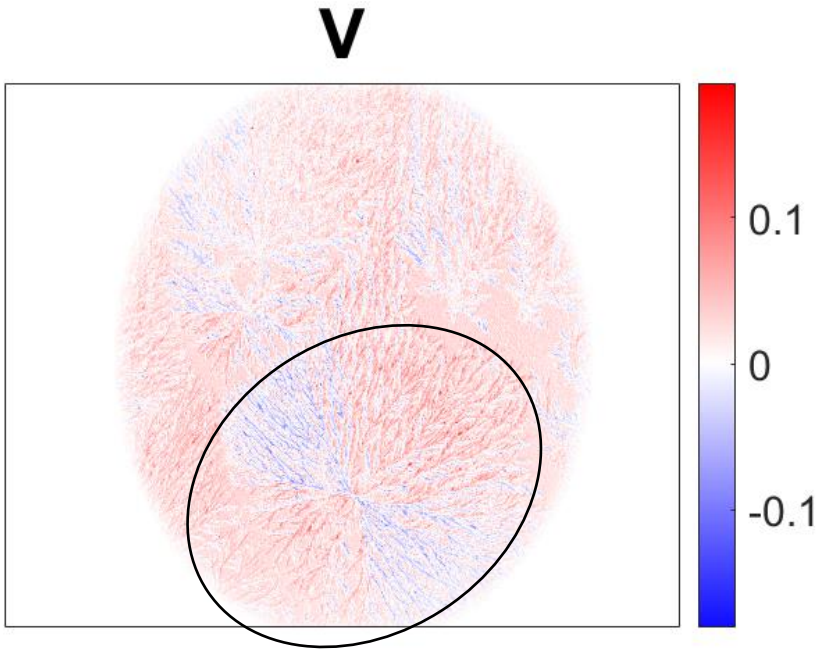

Figure 4.18 : Stokes parameter V image of collagen synthesized at 40 ^{0} C and 9 pH (Circle highlighting the fibril region of interest.)

` For the collagen synthesized at 40 ^{0}C temperature, we see a similar behavior of brighter I and Q (red regions on colormap) image in Figure 4.15 and 4.16 respectively, due to the linearly polarized nature of the background light. We also only see the fiber illumination in case of U and V Stokes parameters (Fig 4.17 and 4.18) as an evidence for the optical activity of the collagen. We can see that the collagen for parameter U (Fig 4.18) is more uniformly spread than the parameter V (Fig 4.17). The fibrils in the highlighted circle in Figure 4.18 have a negative value region (blue) and a positive value region (red). The positive values of V parameter denote the lower amount of retardance resulting in right circularly polarized light. The negative values denote higher retardance in orthogonal axis of polarization resulting in left circularly polarized light. A birefringent material will affect the incoming light differently along its fast axis and slow axis of orientation. If we consider the Figure 4.18 to be a result of birefringence, we can hypothesize that the reason we get a positive value is because the slow axis of the structures is predominantly oriented perpendicular to the incoming light resulting in lower retardance. Similarly, the negative values observed in Figure 4.18 could be a result of the fast axis being predominantly orthogonal to the incoming light polarization resulting in higher retardance. These observations provide a point-by-point analysis on the molecular structural orientation of collagen fibrils. This also reinforces the notion that the collagen polymerization kinetics are due to the nucleation and growth of crystallites originating from the center since we see a similar pattern at the center in case of collagen synthesized at room temperature (Fig 4.11 inset cross). H.E. Oh et. al (2008)., have shown that increasing temperature increases the birefringence and crystalline properties of starch.[80] The temperature difference seems to have affected the retardance properties of collagen here as well and a change in retardance can be observed.

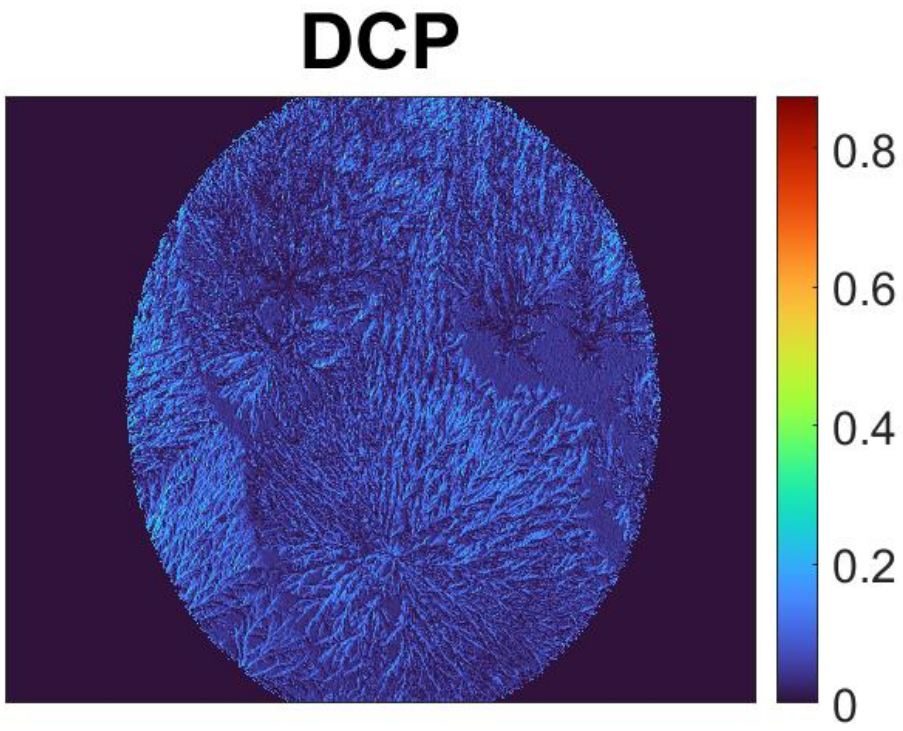

Figure 4.19 : DCP of collagen synthesized at pH 9 and 40 ^{0} C

From the DCP image of collagen synthesized at 40 ^{0} C, it can be observed that almost all of the collagen fibrils from the reference intensity image are visible in the Figure 4.19. There is an absence of regions that are polymerized but not optically active as compared to the images for collagen synthesized at room temperature. This could point to the fact that the collagen is more likely to be birefringent if it is in a fibrillar form due to the molecular alignment and orientation.

Comparing across the samples, we noticed that for the pH range of 7,8, 9 and 10 the collagen architecture looks similar when synthesized at room temperature. We can observe the Maltese cross structures that are described along with a few silent regions that are not illuminated in cross polarized configuration of the microscope. as described in earlier sections (refer Fig 4.7). Similarly, for the pH 7, 8 and 9 we observed a similar trend where the collagen synthesized at 40 ^{0} C showed the branched structure. At pH 10 and 40 ^{0} C, however we noticed that instead of the

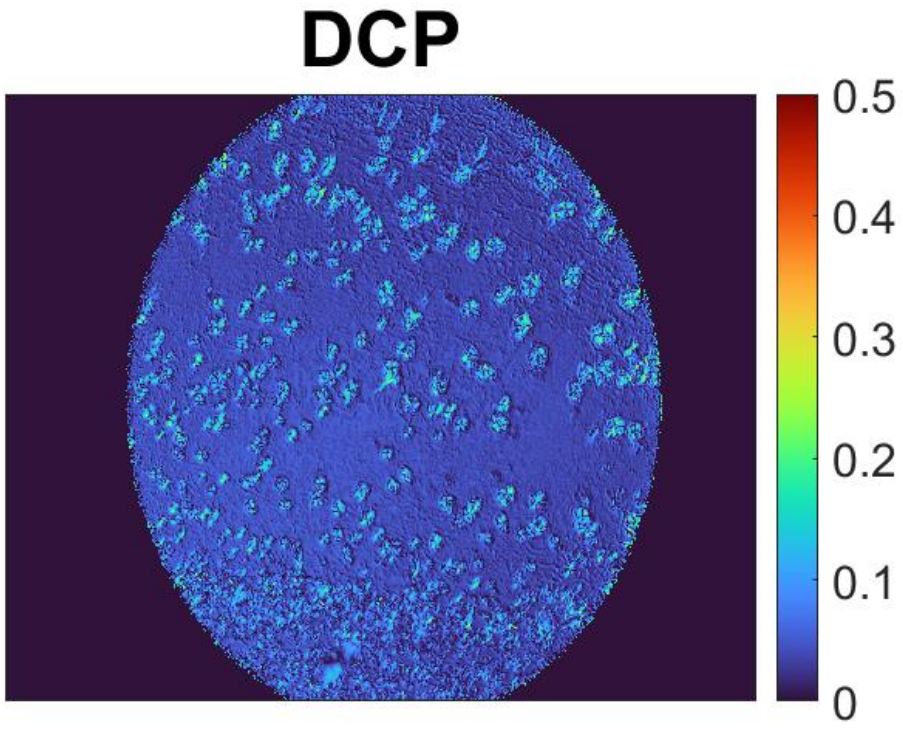

Figure 4.20 : DCP image of collagen synthesized at pH 10 and 40 ^{0}C

branched structure, the collagen formed distorted Maltese cross structures as shown by DCP image in Figure 4.20. These could be because at higher pH and temperature collagen might start losing its triple helical structure. These differences in the pattern would not ordinarily be visible without the use of Stokes parameter measurements.

As observed in this section, PLM and Stokes polarimetry provide information that is not otherwise easily accessible to the researchers. However, each of the hypotheses need an additional supplementary technique characterization like SAXS, DSC etc. for a conclusive evidence. A future study exploring the structural relationship with the optical observations shown here is needed for confirmation of the hypotheses mentioned here.

4.2 PCL

4.2.1 Materials and methods

The poly(ϵ-caprolactone) (PCL) fibers analyzed here were provided by Pokorski lab at UCSD. We would like to thank Professor Jon Pokorski and Justin Hochberg for making the samples available to us. The detailed materials and methods synthesis can be found in Kim et. al. (2017).[81,82] The highly elastic PCL fibers were subjected to a constant uniaxial stress rate to obtain the final strain shown in Figure table 4.1 on an Instron mechanical testing instrument.

Table 4.1: Subjected strain for each of the PCL samples

Sample	Strain
DRM 3	300%
DRM 4	400%
DRM 5	500%
DRM 6	600%

4.2.2 Results and discussions

The PCL images were first conducted using optical microscopy. The optical microscopy images in Figure 4.21 show that all of the PCL fibers are aligned and oriented. The morphological signatures of PCL fibers are similar at 10X magnification as indicated from the figure. The first set of experiments for birefringence were done by calculating the average intensity of PCL fibers when rotated on the stage.

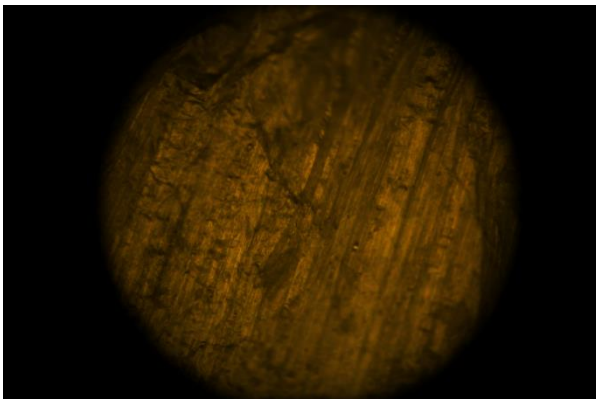

DRM3

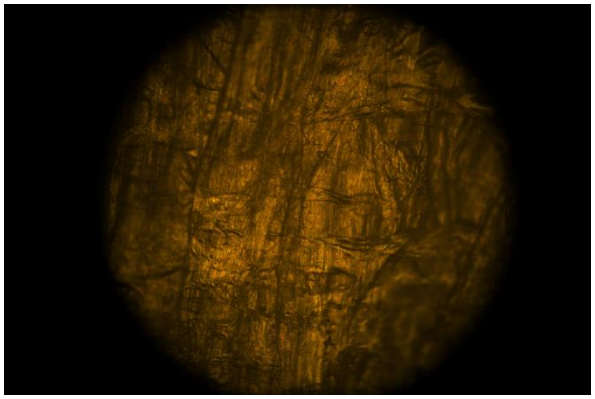

DRM4

DRM5

DRM6

Figure 4.21: DRM optical microscopy images of PCL fibers DRM3, DRM4, DRM5, DRM6

The rotation was carried out on the stage for DRM 3, DRM 6 and a sample on which strain was applied using a vernier caliper. We conducted two sets of experiments for this study. The first set is when the polarizer P2 is removed from the optical path (Fig 4.22- 4.24 unpolarized data) and second when the polarizer P2 is included in the optical path (Fig 4.22-4.24 polarized data). The measurements were conducted at similar starting average intensity values.

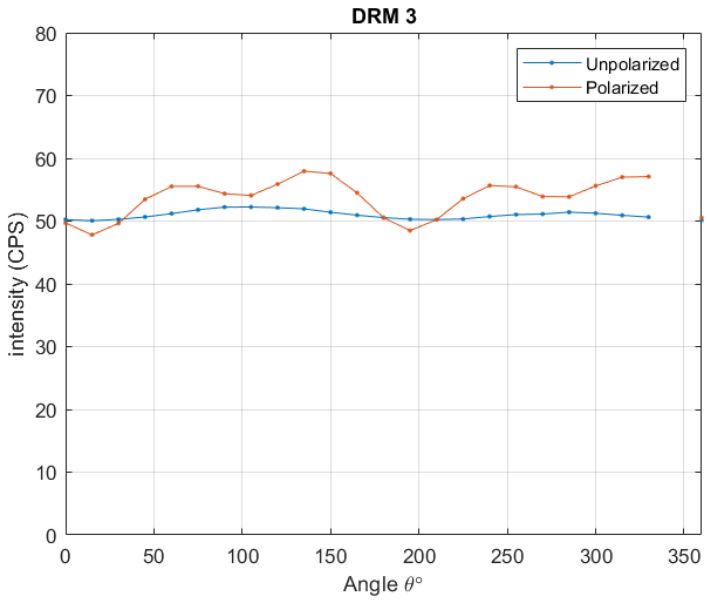

Figure 4.22 : Average intensity measurement of rotation of polarized state and unpolarized states on DRM 3 sample

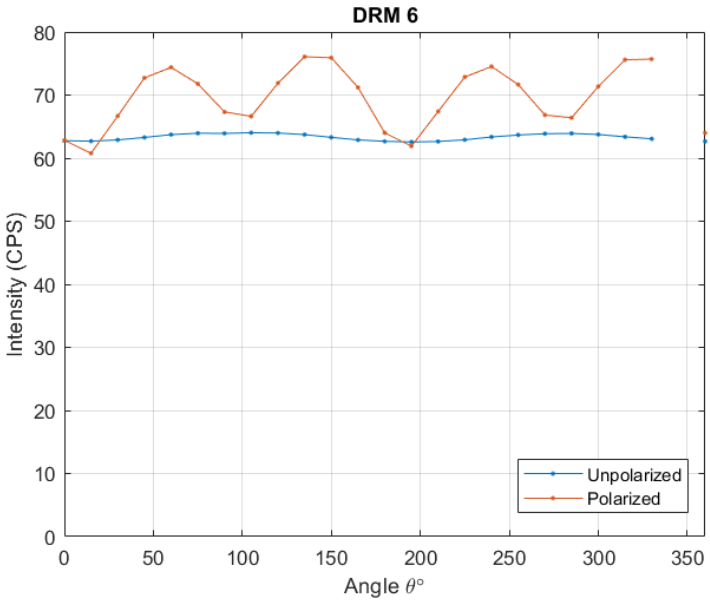

Figure 4.23 : Average intensity measurement of rotation of polarized state and unpolarized states on DRM 6 sample

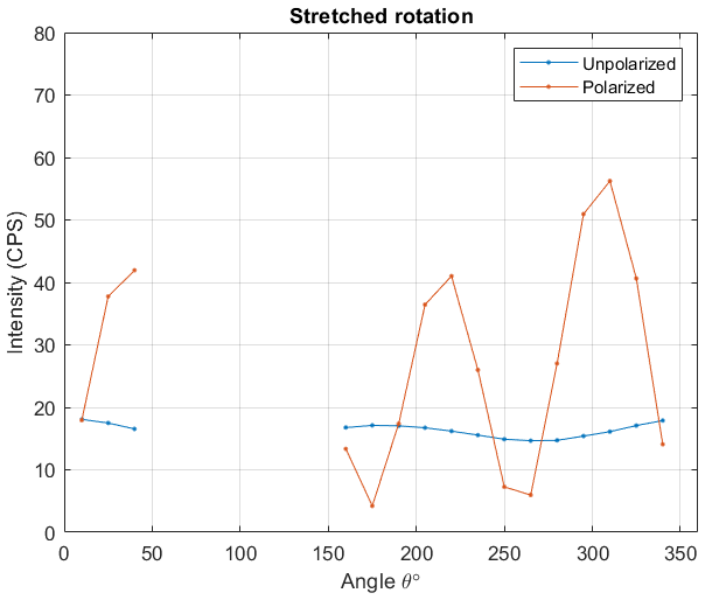

Figure 4.24 : Average intensity measurement of rotation of polarized state and unpolarized states on highly stretched sample

It can be observed from Figures 4.22-4.24 that the average intensity with polarized samples is periodic in nature. We conducted a sinusoidal curve fitting method on above parameters (see Appendix 6.2.2). The periodicity was observed to be approximately π as summarized in table 4.2.

Table 4.2: Table showing the amplitude and period of sinusoidal curve fit data of DRM samples

Sample	Unpolarized Amplitude	Polarized Amplitude	Period
DRM3	2.19	10.16	~π *
DRM6	1.47	15.3	~π *
Stretched rotation	3.41	52.01	~π *

*: The periodicity values are approximate.

The observed periodicity is expected to be at π because the fibers are oriented in a particular direction. If we assume the oriented fibers to be a birefringent material with a fast axis and a slow axis oriented orthogonal to each other, the lowest intensity will be observed when the polarized light components are at an angle somewhere in between the maximum and minimum. This might explain why we can observe a lowest value at approximately in the range of $\frac{\pi}{3}$- $\frac{\pi}{6}$ angle from the highest value in Figure 4.22-4.24 for DRM3, DRM6 and stretched PCL samples. The orientation of fibers and the orientation of incoming light creates an axis where both align and are orthogonal to each other. When the axis of the incoming light and the fast axis of fiber orientation coincide, we see a maximum intensity value peak that is observed in the figures. When the axis of the incoming light coincides with the slow axis, we will see a high peak but, it will be smaller than the highest value and approximately $\frac{\pi}{2}$ from the highest value. This can also be observed in Figure 4.22-4.24 for DRM3, DRM6 and stretched samples.

The reference unpolarized data does not show a similar behavior for observed average intensity. The reason for this kind of behavior can be explained by the anisotropy axis of the fibers. When the sample is excited with linearly polarized light, a birefringent material will allow more light to pass along the axis that is parallel to the vibration plane of fast axis of the birefringent material. As a result, we observe the periodic behavior. The amplitude of the material can also be observed to increase due to an increase in the birefringence of the material for DRM 3 (amplitude ~ 10.16), DRM 6 (amplitude ~15.3) and highly stretched sample (amplitude ~2 52.01). These amplitude changes indicate that an increased amount of strain and alignment results in increase of birefringence of PCL fibers. These observations are in agreement with the previous literature on birefringent polymeric materials [78,83–85] where the source of birefringence is credited to the molecular alignment of polymers. As the strain is increased, the polymer fibrils are more oriented, resulting in higher birefringence.

Following the rotation study, we conducted a Stokes polarimetry study for all of the DRM samples.:

Comparing the Stokes parameters on I, Q, U, V for DRM3 (Fig 4.25), it can be observed that the I image (Fig4.25A) is almost saturated. Which is to be expected due to the background orientation similar to the collagen images. The intensity values in Q image (Fig 4.25B) are positive as compared to that of the negative in the same region for U (Fig 4.25C) and V (Fig 4.35D) image. The PCL samples have comparatively higher thickness than collagen samples observed. It can also be observed that PCL samples have significantly higher opacity. The higher opacity might lead to

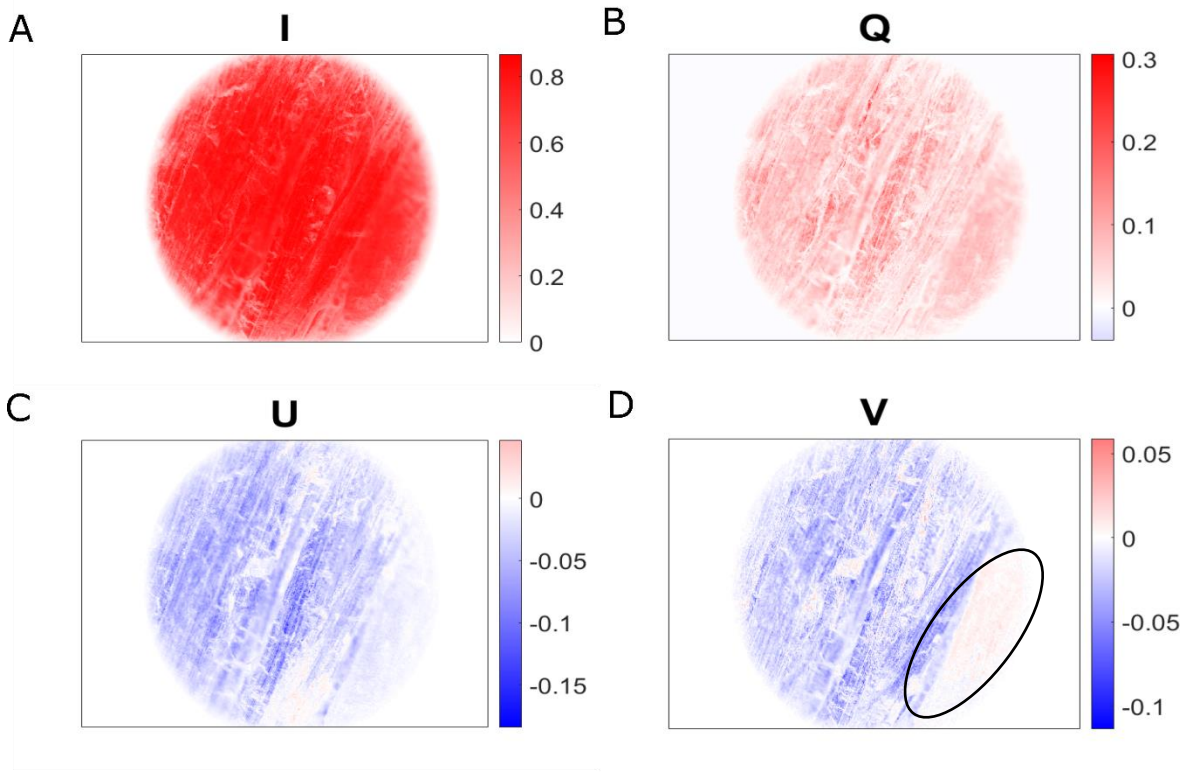

Figure 4.25: Stokes polarimetry images of A) I, B) Q, C) U, D) V parameters of DRM 3 sample. Circle highlighting out of focus region

a more scattering due to its higher opacity. According to Mie theory of scattering, it is observed that for cylindrical objects the photons preserving the polarization tend to scatter in the direction orthogonal to the axis of cylinders.[41,86] This could explain why there U and V parameter values are predominantly negative. However, the out of focus values of V (Fig 4.25 highlighted circle) show a positive value. This could again be a result of either birefringence or scattering. The Stokes parameter measurements for PCL fibers show that the coupling between the scattering due to the structural alignment and the inherent birefringence property need to be resolved for a more comprehensive understanding of the birefringence of PCL fibers. Overall, from a structural point of view, the DRM 3(Fig 4.25), DRM 4(Appendix Fig 6.2), DRM 5(See Appendix 6.3) and DRM 6 (Appendix Fig 6.4), no distinct qualitative pattern was observed. A more quantitative study needs to be conducted to assess the optical properties of PCL fibers. However, for these samples, the

quantitative assessment was proven to be a challenge due to the difficulty to focus on the individual features as result of fibrous nature of the material. As we can observe in Figure 4.25D, the region highlighted is out of focus, and they show a different signature (positive value in this case) for Stokes parameters as compared to the rest of the DRM3 sample.

5. Conclusion, limitations and future perspective

In summary, we demonstrated from chapter 4.1 that synthesized collagen shows optical activity and birefringence that can be characterized by polarized light microscopy. We also demonstrate that the observed Maltese cross patterns are an interference pattern and provide insight onto the birefringence of the material when collagen is synthesized at 20^0 C. The collagen structures show a fibrillar arrangement when synthesized at 40^0 C and seem to grow from the center giving credence to the nucleation and growth theory of spherulites[70,77,78]. We have also demonstrated that almost all of the collagen synthesized at 40^0 C is optically active in nature as opposed to that synthesized at 20 ^{0}C. We have also demonstrated through the Stokes parameter measurements that the collagen starts to structurally change at 40^0 C temperature as we change the pH (observed at 10 pH). From the study conducted for PCL in chapter 4.2 we can summarize that increasing the strain on fibrous material results in an increase in birefringence. The increase in birefringence can be related to the higher molecular alignment of the PCL fibers. We have also demonstrated through V parameter measurement that the scattering plays an important role in highly aligned and significantly opaque PCL fibers.

From Collagen studies conducted in section 4.1, we can conclusively derive that the Stokes polarimetry and PLM provide a rapid spatial analysis of structural properties of material that is not ordinarily accessible using the conventional characterization techniques. Assisted Stokes polarimetry provides an avenue for correlation of the light images to the material properties of the sample in case of birefringent features like Maltese cross structures and fibers. We also demonstrate that the PLM and Stokes parameter study can assist in assessing the kinetics from the structural point of view and can provide important structural information in combination with conventional characterization techniques.

The scattering and turbidity play a major role in polarization propagation of the material. As a result, increased sample thickness and opacity lead to a major limitation where they need to be lower for the Stokes parameter measurements. For the full understanding of the material parameters, a Mueller matrix polarimetry will provide more comprehensive measurement and differentiate between the properties such as diattenuation, birefringence and depolarization which cannot be done using the Stokes polarimetry.[40,41] For the measurement of fibrous thick samples like PCL fibers, it is difficult to obtain images at higher magnification compared to other techniques, which might pose an issue for different Stokes polarimeter analyses.

For future perspective, the Stokes parameter study should be assisted with the conventional XRD and DSC techniques to confirm the hypotheses made here. A full Mueller matrix polarimetry also will be conducted on the samples to verify the validity and degree to which the Stokes parametric measurements can accurately differentiate between the optical anisotropic properties. Broader spectral analyses of the Stokes parameters are also necessary as future steps to further verify the hypotheses and confirm the role of scattering and absorption along with the transmission for the Stokes polarimetry.

6. Appendix

6.1 MATLAB Code

6.1.1 Stokes parameter measurement

```
%read the images and store in the respective matrices.
A = imread('DRM4_0.tif');              %top polarizer at position 0
B = imread('DRM4_45.tif');             %top polarizer at position 45
C = imread('DRM4_90.tif');             %top polarizer at position 90
D = imread('DRM4_135.tif');            %top polarizer at position 135
E = imread('DRM4_no polarizer.tif');           %All polarizers removed
R = imread('0qwp.tif');          %RCP - 0 top polarizer plus qwp in
L = imread('90qwp.tif');         %LCP - 90 top polarizer plus qwp in

% all images read

% Convert to double to get negative values as well
A=im2double(A);
B=im2double(B);
C=im2double(C);
D=im2double(D);
E=im2double(E);
R=im2double(R);
L=im2double(L);

% Stokes parameter calculations
Q=(C-A);
U=(D-B);
V=(L-R);
F=((Q.^2+U.^2).^(1/2))./E;%DOLP calculation
```

```
G=abs(V)./E;%DCP calculation
H=((Q.^2+U.^2+V.^2).^(1/2))./E;%DOP calculation

%Individual figures of each plot.
figure,imshow(A);title('0');
figure,imshow(B);title('45');
figure,imshow(C);title('90');
figure,imshow(D);title('135');
figure,imshow(E);title('no polarization'); % First Stokes parameter
figure,imshow(Q);title('Q');colorbar; % Second Stokes parameter
figure,imshow(U);title('U');colorbar; % Third Stokes parameter
figure,imshow(V);title('V');colorbar; % Fourth Stokes parameter
figure,imshow(F);title('DOLP');colorbar; % Degree of linear polarization
figure,imshow(G);title('DCP');colorbar; % Degree of circular polarization
figure,imshow(H);title('DOP');colorbar; % degree of polarization


%Save the data
mkdir('Stokes parameters')

mkdir('Stokes parameters/RGB')
imwrite(Q,'Stokes parameters/RGB/Q.jpg','jpg');
imwrite(U,'Stokes parameters/RGB/U.jpg','jpg');
imwrite(V,'Stokes parameters/RGB/V.jpg','jpg');
imwrite(F,'Stokes parameters/RGB/DOLP.jpg','jpg');
imwrite(G,'Stokes parameters/RGB/DCP.jpg','jpg');
imwrite(H,'Stokes parameters/RGB/DOP.jpg','jpg');

imwrite(G3,'Stokes parameters/B/DCPB.jpg','jpg');
```

```
imwrite(H3,'Stokes parameters/B/DOPB.jpg','jpg');


%Data range must be from 0 to 1
datarangeF=[min(F(:)) max(F(:))];
datarangeG=[min(G(:)) max(G(:))];
datarangeH=[min(H(:)) max(H(:))];
```

6.1.2 MATLAB code Sinosoidal curve fit

```
x=SRA;
y=SRU;
yu = max(y);
yl = min(y);
yr = (yu-yl);                          % Range of 'y'
yz = y-yu+(yr/2);
zx = x(yz .* circshift(yz,[0 1]) <= 0);     % Find zero-crossings
per = 2*mean(diff(zx));                    % Estimate period
ym = mean(y);                              % Estimate offset
fit = @(b,x)  b(1).*(sin(2*pi*x./b(2) + 2*pi/b(3))) + b(4);    % Function to fit
fcn = @(b) sum((fit(b,x) - y).^2);                             % Least-Squares cost function
s = fminsearch(fcn, [yr;  per;  -1;  ym])                    % Minimise Least-Squares
xp = linspace(min(x),max(x));
figure(1)
plot(x,y,'b',  xp,fit(s,xp), 'r')
grid
```

6.2 Collagen images without correction:

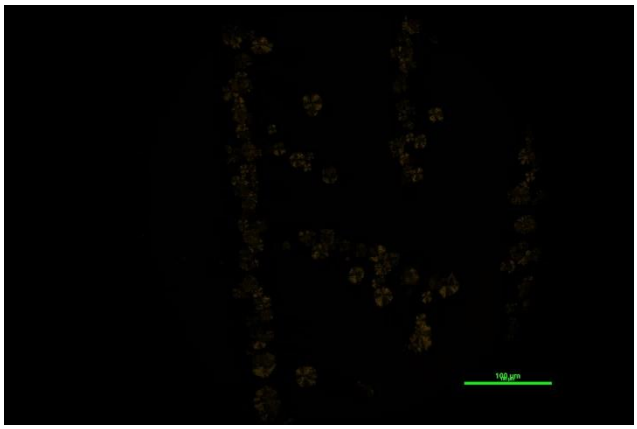

Figure 6.1: Raw image for Figure 4.6

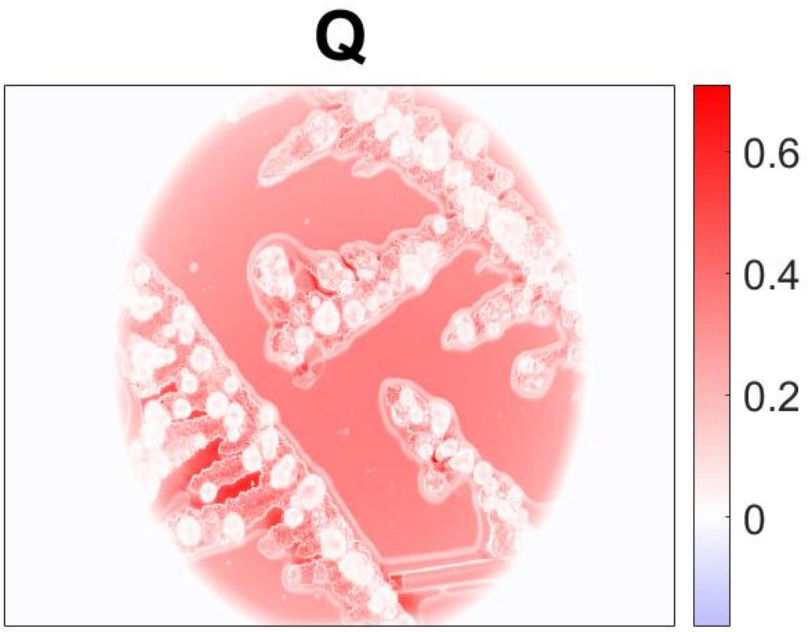

Figure 6.2: Raw image for Figure 4.9

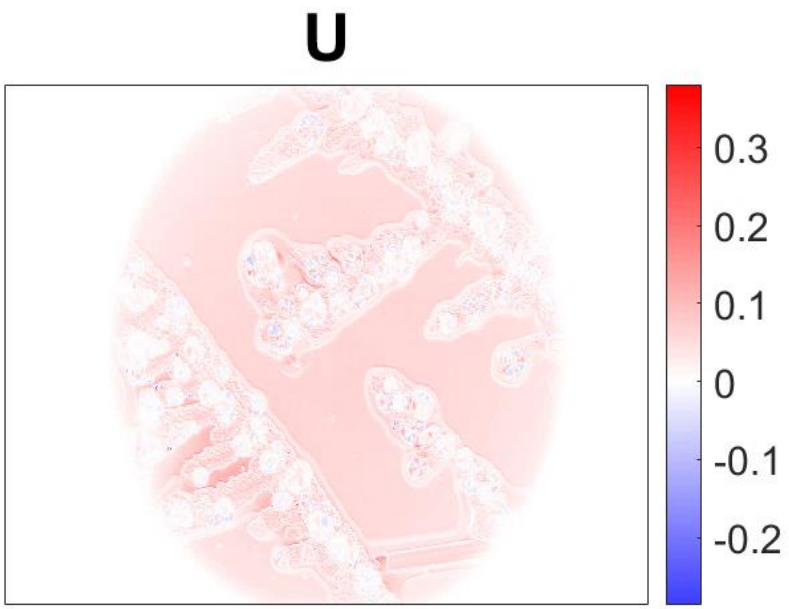

Figure 6.3: Raw image for figure 4.10

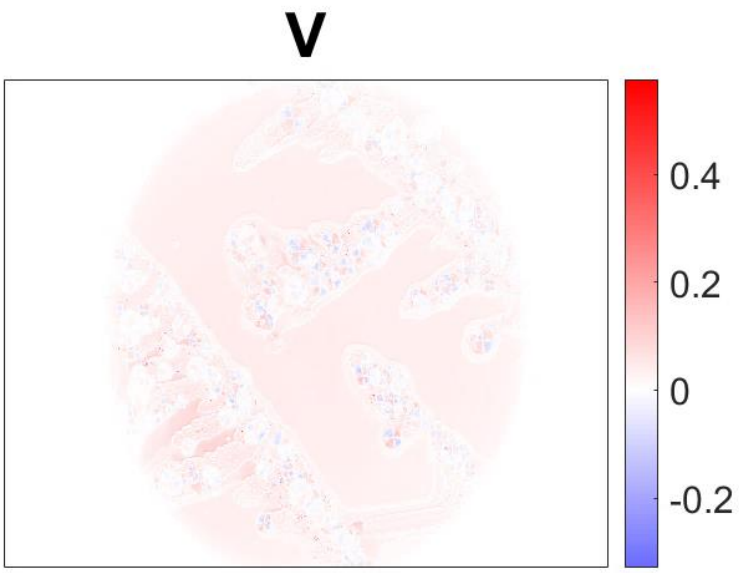

Figure 6.4: Raw image for figure 4.10

6.3 PCL fiber images.

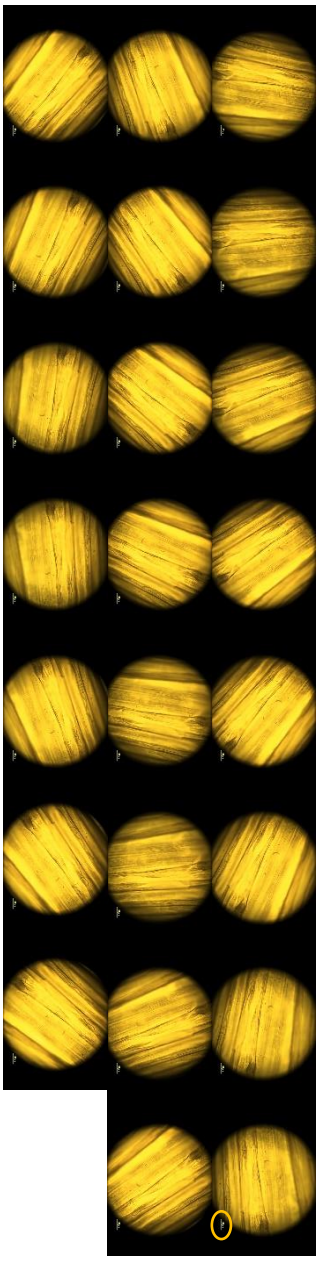

Figure 6.5: An example images for rotation images of PCL fibers at DRM 6 from 0^0 to 300^0 at an interval of 15^0

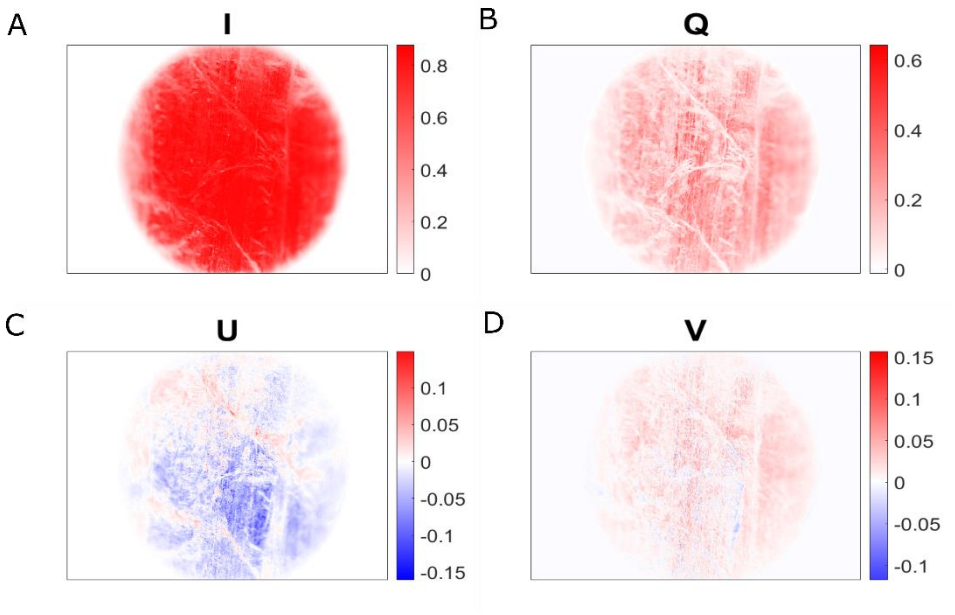

Figure 6.6: Images of Stokes polarimetry parameters I, Q, U, V for DRM 4 PCL fibers

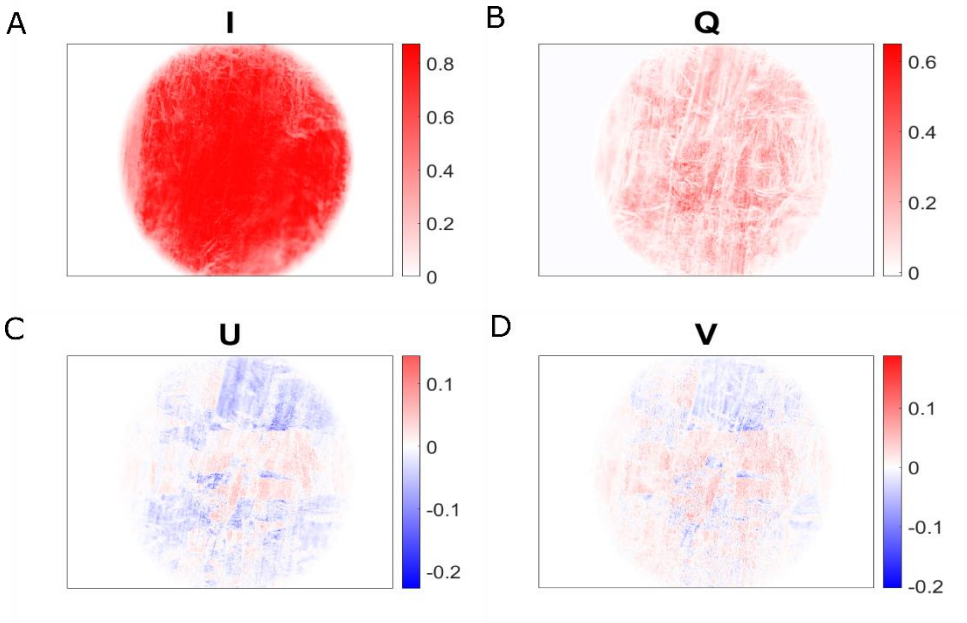

Figure 6.7: Images of Stokes polarimetry parameters I, Q, U, V for DRM 5 PCL fibers

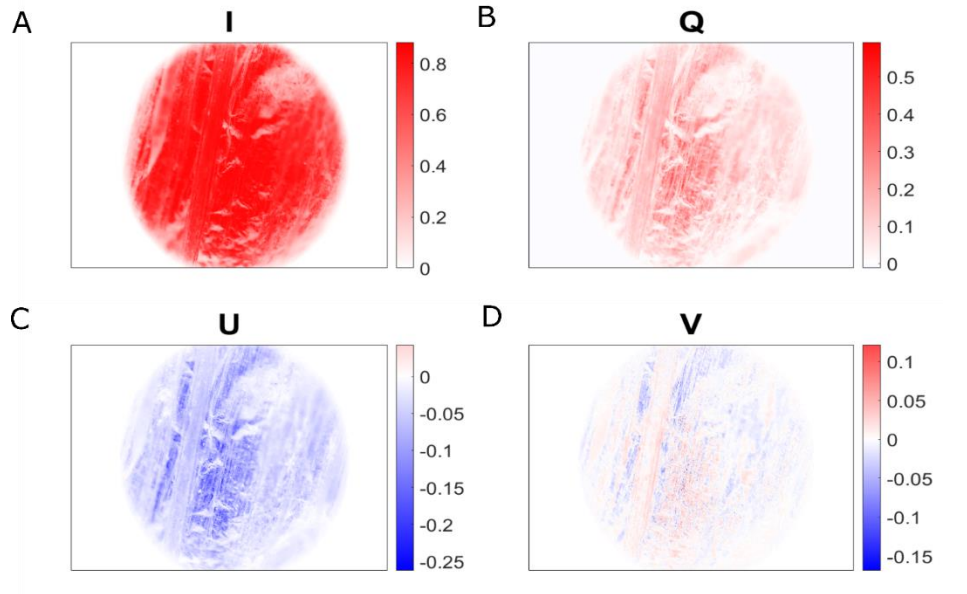

Figure 6.8: Images of Stokes polarimetry parameters I, Q, U, V for DRM 6 PCL fiber

6.4 Supplementary videos

Supplemental video 1: Puri_01_rotation.wav

Supplemental video 2: Puri_02_rotation.wav

7. References

[1] N. Raval, R. Maheshwari, D. Kalyane, S.R. Youngren-Ortiz, M.B. Chougule, R.K. Tekade, Importance of Physicochemical Characterization of Nanoparticles in Pharmaceutical Product Development, Basic Fundam. Drug Deliv. (2019) 369–400. https://doi.org/10.1016/B978-0-12-817909-3.00010-8.

[2] M.K. Abolfazl, T. Kobra, C. Shahla, J.M. Taghi, M. Fatemeh, T.S. Mohammad, M.N.A. Sadat, L. Nasrin, P.B. Shahram, F.A.Y. Abbas, A.S. Mehr, How to prepare biological samples and live tissues for scanning electron microscopy (SEM) (review article), gmj. 3 (2014) 63–80. Https://www.sid.ir/en/journal/viewpaper.aspx?id=435436 (accessed august 4, 2021).

[3] R. Aston, K. Sewell, T. Klein, G. Lawrie, L. Grøndahl, Evaluation of the impact of freezing preparation techniques on the characterisation of alginate hydrogels by cryo-SEM, Eur. Polym. J. 82 (2016) 1–15. https://doi.org/10.1016/J.EURPOLYMJ.2016.06.025.

[4] N.A. Sutton, N. Hughes, P.S. Handley, A comparison of conventional SEM techniques, low temperature SEM and the electroscan wet scanning electron microscope to study the structure of a biofilm of Streptococcus crista CR3, J. Appl. Bacteriol. 76 (1994) 448–454. https://doi.org/10.1111/J.1365-2672.1994.TB01101.X.

[5] B.R. Masters, P.T.C. So, E. Gratton, Multiphoton Excitation Microscopy and Spectroscopy of Cells, Tissues and Human Skin In Vivo, Fluoresc. Lumin. Probes Biol. Act. (1999) 414–432. https://doi.org/10.1016/B978-012447836-7/50033-6.

[6] C. Ricard, J.A. Coles, R. Serduc, B. van der Sanden, P. Verant, J.C. Vial, Two-Photon Imaging, Encycl. Neurosci. (2009) 1221–1229. https://doi.org/10.1016/B978-008045046-9.00863-9.

[7] M. Kitano, T. Okada, Four-Dimensional Tracking of Lymphocyte Migration and Interactions in Lymph Nodes by Two-Photon Microscopy, Methods Enzymol. 506 (2012) 437–454. https://doi.org/10.1016/B978-0-12-391856-7.00047-0.

[8] P.P. Provenzano, D.R. Inman, K.W. Eliceiri, J.G. Knittel, L. Yan, C.T. Rueden, J.G. White, P.J. Keely., Collagen density promotes mammary tumor initiation and progression, BMC Med. 6 (2008). https://doi.org/10.1186/1741-7015-6-11.

[9] W.R. Zipfel, R.M. Williams, R. Christie, A.Y. Nikitin, B.T. Hyman, W.W. Webb, Live tissue intrinsic emission microscopy using multiphoton-excited native fluorescence and second harmonic generation, Proc. Natl. Acad. Sci. U. S. A. 100 (2003) 7075–7080. https://doi.org/10.1073/PNAS.0832308100.

[10] P.P. Provenzano, K.W. Eliceiri, J.M. Campbell, D.R. Inman, J.G. White, P.J. Keely, Collagen reorganization at the tumor-stromal interface facilitates local invasion, BMC Med.

4 (2006) 38. https://doi.org/10.1186/1741-7015-4-38.

[11] M. Müller, A. Zumbusch, Coherent anti-Stokes Raman Scattering Microscopy, ChemPhysChem. 8 (2007) 2156–2170. https://doi.org/10.1002/CPHC.200700202.

[12] J.J.A. Poole, L.B. Mostaço-Guidolin, Optical Microscopy and the Extracellular Matrix Structure: A Review, Cells 2021, Vol. 10, Page 1760. 10 (2021) 1760. https://doi.org/10.3390/CELLS10071760.

[13] J. Adur, H.F. Carvalho, C.L. Cesar, V. H.Casco, Nonlinear Microscopy Techniques: Principles and Biomedical Applications, Microsc. Anal. (2016). https://doi.org/10.5772/63451.

[14] 2.4: Staining Microscopic Specimens - Biology LibreTexts, (n.d.). https://bio.libretexts.org/Bookshelves/Microbiology/Microbiology_(OpenStax)/02%3A_How_We_See_the_Invisible_World/2.04%3A_Staining_Microscopic_Specimens (accessed August 4, 2021).

[15] R.W. CAHN, RECOVERY AND RECRYSTALLIZATION, Phys. Metall. (1996) 2399–2500. https://doi.org/10.1016/B978-044489875-3/50033-8.

[16] V. Moody, H.L. Needles, Fiber Identification and Characterization, Tufted Carpet. (2004) 23–34. https://doi.org/10.1016/B978-188420799-0.50003-8.

[17] K. Katoh, K. Hammar, P.J.S. Smith, R. Oldenbourg, Arrangement of radial actin bundles in the growth cone of Aplysia bag cell neurons shows the immediate past history of filopodial behavior, Proc. Natl. Acad. Sci. U. S. A. 96 (1999) 7928. https://doi.org/10.1073/PNAS.96.14.7928.

[18] S. Simoes, Y. Oh, M.F.Z. Wang, R. Fernandez-Gonzalez, U. Tepass, Myosin II promotes the anisotropic loss of the apical domain during Drosophila neuroblast ingression, J. Cell Biol. 216 (2017) 1387–1404. https://doi.org/10.1083/JCB.201608038.

[19] R. Loganathan, B.R. Potetz, B.J. Rongish, C.D. Little, Spatial Anisotropies and Temporal Fluctuations in Extracellular Matrix Network Texture during Early Embryogenesis, PLoS One. 7 (2012) e38266. https://doi.org/10.1371/JOURNAL.PONE.0038266.

[20] T.E. Sztal, C. Sonntag, T.E. Hall, P.D. Currie, Epistatic dissection of laminin–receptor interactions in dystrophic zebrafish muscle, Hum. Mol. Genet. 21 (2012) 4718–4731. https://doi.org/10.1093/HMG/DDS312.

[21] B. Penke, G. Paragi, J. Gera, R. Berkecz, Z. Kovács, T. Crul, L. Vígh, The Role of Lipids and Membranes in the Pathogenesis of Alzheimer's Disease: A Comprehensive View, Curr. Alzheimer Res. 15 (2018) 1191–1212. https://doi.org/10.2174/1567205015666180911151716.

[22] L.-W. Jin, K.A. Claborn, M. Kurimoto, M.A. Geday, I. Maezawa, F. Sohraby, M. Estrada, W. Kaminksy, B. Kahr, Imaging linear birefringence and dichroism in cerebral amyloid pathologies, 100 (2003) 2021. www.metripol.com (accessed July 17, 2021).

[23] W. Kaminksy, L-W Jin, S. Powell, I. Maezawa, K. Claborn, C. Branham, B. Kahr, Polarimetric imaging of amyloid, Micron. 37 (2006) 324–338. https://doi.org/10.1016/J.MICRON.2005.10.014.

[24] A.G. Nerlich, M.L. Nerlich, P.K. Müller, Pattern of collagen types and molecular structure of collagen in acute post-traumatic pulmonary fibrosis., Thorax. 42 (1987) 863. https://doi.org/10.1136/THX.42.11.863.

[25] K.M. Mak, C.Y. Png, D.J. Lee, Type V Collagen in Health, Disease, and Fibrosis, Anat. Rec. (Hoboken). 299 (2016) 613–629. https://doi.org/10.1002/AR.23330.

[26] T. Saneyasu, S. Yoshioka, T. Sakai, Mechanisms of Collagen Network Organization in Response to Tissue/Organ Damage, Compos. Funct. Extracell. Matrix Hum. Body. (2016). https://doi.org/10.5772/63163.

[27] K.M. Riching, B.L. Cox, M.R. Salick, C. Pehlke, A.S. Riching, S.M. Ponik, B.R. Bass, W.C. Crone, Y. Jiang, A.M. Weaver, K.W. Eliceiri, P.J. Keely, 3D collagen alignment limits protrusions to enhance breast cancer cell persistence, Biophys. J. 107 (2015) 2546–2558. https://doi.org/10.1016/j.bpj.2014.10.035.

[28] D.A. Landry, H.T. Vaishnav, B.C. Vanderhyden, The significance of ovarian fibrosis, Oncotarget. 11 (2020) 4366–4370. https://doi.org/10.18632/ONCOTARGET.27822.

[29] N.A. Mcbrien, R. Metlapally, A.I. Jobling, A. Gentle, Expression of Collagen-Binding Integrin Receptors in the Mammalian Sclera and Their Regulation during the Development of Myopia, 47 (2006) 4674–4682. https://doi.org/10.1167/iovs.05-1150.

[30] J.K. Pijanka, B. Coudrillier, K. Ziegler, T. Sorensen, K.M. Meek, T.D. Nguyen, H.A. Quigley, C. Boote, Quantitative Mapping of Collagen Fiber Orientation in Non-glaucoma and Glaucoma Posterior Human Sclerae, Invest. Ophthalmol. Vis. Sci. 53 (2012) 5258–5270. https://doi.org/10.1167/IOVS.12-9705.

[31] H.J.C. de Vries, D.N.H. Enomoto, J. van Marle, P.P.M. van Zuijlen, J.R. Mekkes, J.D. Bos, Dermal Organization in Scleroderma: The Fast Fourier Transform and the Laser Scatter Method Objectify Fibrosis in Nonlesional as well as Lesional Skin, Lab. Investig. 2000 808. 80 (2000) 1281–1289. https://doi.org/10.1038/labinvest.3780136.

[32] J. M, Mechanisms of skin fibrosis in systemic sclerosis, J. Dermatol. 37 (2010) 11–25. https://doi.org/10.1111/J.1346-8138.2009.00738.X.

[33] A.N. Yaroslavsky, J.G. Barbosa, V. Neel, C.A. DiMarzio, R.R.A. M.D., Combining

multispectral polarized light imaging and confocal microscopy for localization of nonmelanoma skin cancer, J. Biomed. Opt. 10 (2005) 014011. https://doi.org/10.1117/1.1854173.

[34] A. Zoumi, A. Yeh, B.J. Tromberg, Imaging cells and extracellular matrix in vivo by using second-harmonic generation and two-photon excited fluorescence, Proc. Natl. Acad. Sci. U. S. A. 99 (2002) 11014–11019. https://doi.org/10.1073/PNAS.172368799.

[35] C.E. Shieh, Y.-F. Chen, The Application of Polarized Light Microscopy to Identify Minerals-A Preliminary Study of Forensic Geology, FORENSIC Sci. J. SINCE 2002 Forensic Sci. J. 12 (2013) 15–30.

[36] M.W. Davidson, G.E. Lofgren, Photomicrography in the geological sciences, J. Geol. Educ. 39 (1991) 403–418. https://doi.org/10.5408/0022-1368-39.5.403.

[37] L.A. Muñoz, F. Pedreschi, A. Leiva, J.M. Aguilera, Loss of birefringence and swelling behavior in native starch granules: Microstructural and thermal properties, J. Food Eng. 152 (2015) 65–71. https://doi.org/10.1016/J.JFOODENG.2014.11.017.

[38] C. Ortuño, A. Quiles, J. Benedito, Inactivation kinetics and cell morphology of E. coli and S. cerevisiae treated with ultrasound-assisted supercritical CO2, Food Res. Int. 62 (2014) 955–964. https://doi.org/10.1016/J.FOODRES.2014.05.012.

[39] A.S. Jääskeläinen, U. Holopainen-Mantila, T. Tamminen, T. Vuorinen, Endosperm and aleurone cell structure in barley and wheat as studied by optical and Raman microscopy, J. Cereal Sci. 57 (2013) 543–550. https://doi.org/10.1016/J.JCS.2013.02.007.

[40] N. Ghosh, M.F.G. Wood, S. Li, R.D. Weisel, B.C. Wilson, R.-K. Li, I.A. Vitkin, Mueller matrix decomposition for polarized light assessment of biological tissues, J. Biophotonics. 2 (2009) 145–156. https://doi.org/10.1002/jbio.200810040.

[41] H. He, N. Zeng, E. Du, Y. Guo, D. Li, R. Liao, Y. He, H. Ma, Two-dimensional and surface backscattering Mueller matrices of anisotropic sphere-cylinder scattering media: a quantitative study of influence from fibrous scatterers, J. Biomed. Opt. 18 (2013) 046002. https://doi.org/10.1117/1.JBO.18.4.046002.

[42] E. Du, H. He, N. Zeng, M. Sun, Y. Guo, J. Wu, S. Liu, H. Ma, Mueller matrix polarimetry for differentiating characteristic features of cancerous tissues, J. Biomed. Opt. 19 (2014) 076013. https://doi.org/10.1117/1.jbo.19.7.076013.

[43] S.-Y. Lu, R.A. Chipman, Interpretation of Mueller matrices based on polar decomposition, J. Opt. Soc. Am. A. 13 (1996) 1106. https://doi.org/10.1364/josaa.13.001106.

[44] E. Du, H. He, N. Zeng, Y. Guo, R. Liao, Y. He, H. Ma, Two-dimensional backscattering Mueller matrix of sphere-cylinder birefringence media, J. Biomed. Opt. 17 (2012) 126016.

https://doi.org/10.1117/1.JBO.17.12.126016.

[45] P. Whittaker, R.A. Kloner, D.R. Boughner, J.G. Pickering, Quantitative assessment of myocardial collagen with picrosirius red staining and circularly polarized light, Basic Res. Cardiol. 89 (1994) 397–410. https://doi.org/10.1007/BF00788278.

[46] L-W. Jin, K.A. Claborn, M. Kurimoto, M.A. Geday, I. Maezawa, F. Sohraby, M. Estrada, W. Kaminksy, B. Kahr, Imaging linear birefringence and dichroism in cerebral amyloid pathologies, Proc. Natl. Acad. Sci. U. S. A. 100 (2003) 15294–15298. https://doi.org/10.1073/PNAS.2534647100.

[47] E.S.A. Goerlitzer, A.S. Puri, J.J. Moses, L. V. Poulikakos, N. Vogel, The Beginner's Guide to Chiral Plasmonics: Mostly Harmless Theory and the Design of Large-Area Substrates, Adv. Opt. Mater. (2021) 2100378. https://doi.org/10.1002/ADOM.202100378.

[48] E. Collett, Polarized light. Fundamentals and applications., in: Plfa, 1992.

[49] E. Collett, Field Guide to Polarization, 2009. https://doi.org/10.1117/3.626141.

[50] J.C. Kemp, Polarized Light and its Interaction with Modulating Devices-a Methodology Review-Polarized Light and Its Interaction With Modulating Devices, 1987.

[51] Absorption and Scattering of Light by Small Particles - Craig F. Bohren, Donald R. Huffman - Google Books, (n.d.). https://books.google.com/books?hl=en&lr=&id=ib3EMXXIRXUC&oi=fnd&pg=PP2&ots=AAavA9gcXK&sig=y0J1o7ygi_AxVggWiSWy7Ngl-N4 (accessed December 24, 2020).

[52] S.N. Savenkov, Jones and Mueller matrices: structure, symmetry relations and information content, in: Light Scatt. Rev. 4, Springer Berlin Heidelberg, 2009: pp. 71–119. https://doi.org/10.1007/978-3-540-74276-0_3.

[53] H. Pinto, R. Jones, J.P. Goss, Theory of the birefringence due to dislocations in single crystal CVD diamond, J. Phys. Condens. Matter. (2009). https://doi.org/10.1088/0953-8984/21/36/364220.

[54] M.P. Silverman, R.B. Sohn, Effects of circular birefringence on light propagation and reflection, Cit. Am. J. Phys. 54 (1986) 69. https://doi.org/10.1119/1.14745.

[55] M. Ren, E. Plum, J. Xu, I. Zheludev, Giant nonlinear optical activity in a plasmonic metamaterial, Nat. Commun. (2012). https://doi.org/10.1038/ncomms1805.

[56] A. V. Poshakinskiy, D.R. Kazanov, T. V. Shubina, S.A. Tarasenko, Optical activity in chiral stacks of 2D semiconductors, Nanophotonics. 7 (2018) 753–762. https://doi.org/10.1515/nanoph-2017-0114.

[57] Y. Kato, T. Teraji, 4 Key technologies for device fabrications and materials characterizations 4.1 Characterization methods of defects in single crystalline diamond for power device application, (2018). https://doi.org/10.1016/B978-0-08-102183-5.00004-2.

[58] Linear Dichroism and Circular Dichroism, n.d.

[59] Photoelastic modulators Stokes Polarimetry Technology for Polarization Measurement, (2000). www.hindsinstruments.com (accessed August 25, 2021).

[60] C. Xu, J. Ma, C. Ke, Y. Huang, Z. Zeng, W. Weng, L. Shen, K. Wang, Full-Stokes polarization imaging based on liquid crystal variable retarders and metallic nanograting arrays, J. Phys. D. Appl. Phys. 53 (2020) 015112. https://doi.org/10.1088/1361-6463/ab4ba0.

[61] M. Ikram, S. Firdous, M. Ikram, M. Ikram, Stokes Polarimetry for the Characterization of Bio-Materials using Liquid Crystal Variable Retarders, Ther. Laser Appl. Laser-Tissue Interact. III (2007), Pap. 6632_14. (2007) 6632_14. https://doi.org/10.1364/ECBO.2007.6632_14.

[62] W. YL, Z. R, W. ZB, W. TD, L. KW, [A New Strategy of Spectrum and Polarization Measuring based on LCVR and AOTF]., Guang Pu Xue Yu Guang Pu Fen Xi. 35 (2015) 2362–2367. https://europepmc.org/article/med/26672326 (accessed August 9, 2021).

[63] A. Pors, M.G. Nielsen, S.I. Bozhevolnyi, Plasmonic metagratings for simultaneous determination of Stokes parameters, Opt. Vol. 2, Issue 8, Pp. 716-723. 2 (2015) 716–723. https://doi.org/10.1364/OPTICA.2.000716.

[64] L. Li, J. Wang, L. Kang, W. Liu, L. Yu, B. Zheng, M.L. Brongersma, D.H. Werner, S. Lan, Y. Shi, Y. Xu, X. Wang, Monolithic Full-Stokes Near-Infrared Polarimetry with Chiral Plasmonic Metasurface Integrated Graphene-Silicon Photodetector, ACS Nano. 14 (2020) 16634–16642. https://doi.org/10.1021/acsnano.0c00724.

[65] E. Arbabi, S.M. Kamali, A. Arbabi, A. Faraon, Full-Stokes Imaging Polarimetry Using Dielectric Metasurfaces, ACS Photonics. 5 (2018) 3132–3140. https://doi.org/10.1021/ACSPHOTONICS.8B00362.

[66] G.C. Giakos, S.A. Paturi, P. Bathini, S. Sukumar, K. Ambadipudi, K. Valium, D. Wagenar, V. Adya, M. Reddy, New pathways towards the enhancement of the image quality, Conf. Rec. - IEEE Instrum. Meas. Technol. Conf. (2007). https://doi.org/10.1109/IMTC.2007.379461.

[67] C.I. Osorio, A. Mohtashami, A.F. Koenderink, K-space polarimetry of bullseye plasmon antennas, Sci. Reports 2015 51. 5 (2015) 1–7. https://doi.org/10.1038/srep09966.

[68] J.A. Paten, G.E. Tilburey, E.A. Molloy, R. Zareian, C. V. Trainor, J.W. Ruberti, Utility of

an optically-based, micromechanical system for printing collagen fibers, Biomaterials. 34 (2013) 2577. https://doi.org/10.1016/J.BIOMATERIALS.2012.12.028.

[69] J.Y. Dewavrin, N. Hamzavi, V.P.W. Shim, M. Raghunath, Tuning the architecture of three-dimensional collagen hydrogels by physiological macromolecular crowding, Acta Biomater. 10 (2014) 4351–4359. https://doi.org/10.1016/J.ACTBIO.2014.06.006.

[70] Y. Wang, T. Azaïs, M. Robin, A. Vallée, C. Catania, P. Legriel, G. Pehau-Arnaudet, F. Babonneau, M.-M. Giraud-Guille, N. Nassif, The predominant role of collagen in the nucleation, growth, structure and orientation of bone apatite, Nat. Mater. 2012 118. 11 (2012) 724–733. https://doi.org/10.1038/nmat3362.

[71] S. Elsharkawy, M. Al-Jawad, M.F. Pantano, E. Tejeda-Montes, K. Mehta, H. Jamal, S. Agarwal, K. Shuturminska, A. Rice, N. V Tarakina, R.M. Wilson, A.J. Bushby, M. Alonso, J.C. Rodriguez-Cabello, E. Barbieri, A. Del Río Hernández, M.M. Stevens, N.M. Pugno, P. Anderson, A. Mata, Protein disorder-order interplay to guide the growth of hierarchical mineralized structures, (n.d.). https://doi.org/10.1038/s41467-018-04319-0.

[72] W. Błaszczak, G. Lewandowicz, Light microscopy as a tool to evaluate the functionality of starch in food, Foods. 9 (2020) 1–15. https://doi.org/10.3390/foods9050670.

[73] Y. Ai, J.L. Jane, Understanding Starch Structure and Functionality, Starch Food Struct. Funct. Appl. Second Ed. (2018) 151–178. https://doi.org/10.1016/B978-0-08-100868-3.00003-2.

[74] S. Jagadeesan, I. Govindaraju, N. Mazumder, An Insight into the Ultrastructural and Physiochemical Characterization of Potato Starch: a Review, Am. J. Potato Res. 97 (2020) 464–476. https://doi.org/10.1007/S12230-020-09798-W.

[75] J. Shi, M.C. Sweedman, Y.C. Shi, Structure, birefringence and digestibility of spherulites produced from debranched waxy maize starch, Int. J. Biol. Macromol. 183 (2021) 1486–1494. https://doi.org/10.1016/J.IJBIOMAC.2021.05.127.

[76] W.D. Comper, A. Veis, The mechanism of nucleation for in vitro collagen fibril formation, Biopolymers. 16 (1977) 2113–2131. https://doi.org/10.1002/BIP.1977.360161004.

[77] Y. Liu, Y.K. Kim, L. Dai, N. Li, S.O. Khan, D.H. Pashley, F.R. Tay, Hierarchical and non-hierarchical mineralisation of collagen, Biomaterials. 32 (2011) 1291–1300. https://doi.org/10.1016/J.BIOMATERIALS.2010.10.018.

[78] A. Tagaya, Y. Koike, Compensation and control of the birefringence of polymers for photonics, Polym. J. 2012 444. 44 (2012) 306–314. https://doi.org/10.1038/pj.2011.141.

[79] S. Elsharkawy, M. Al-Jawad, M.F. Pantano, E. Tejeda-Montes, K. Mehta, H. Jamal, S. Agarwal, K. Shuturminska, A. Rice, N. V Tarakina, R.M. Wilson, A.J. Bushby, M. Alonso,

J.C. Rodriguez-Cabello, E. Barbieri, A. Del Río Hernández, M.M. Stevens, N.M. Pugno, P. Anderson, A. Mata, Protein disorder-order interplay to guide the growth of hierarchical mineralized structures, (n.d.). https://doi.org/10.1038/s41467-018-04319-0.

[80] H.E. Oh, D.N. Pinder, Y. Hemar, S.G. Anema, M. Wong, Effect of high-pressure treatment on various starch-in-water suspensions, Food Hydrocoll. 22 (2008) 150–155. https://doi.org/10.1016/J.FOODHYD.2007.01.028.

[81] A.M. Jordan, L.T.J. Korley, Toward a Tunable Fibrous Scaffold: Structural Development during Uniaxial Drawing of Coextruded Poly(ε-caprolactone) Fibers, Macromolecules. 48 (2015) 2614–2627. https://doi.org/10.1021/ACS.MACROMOL.5B00370.

[82] S.-E. Kim, A.M. Jordan, L.T.J. Korley, J.K. Pokorski, Drawing in poly(ε-caprolactone) fibers: tuning mechanics, fiber dimensions and surface-modification density, J. Mater. Chem. B. 5 (2017) 4499–4506. https://doi.org/10.1039/C7TB00096K.

[83] C. Baptista, A. Azagury, H. Shin, C.M. Baker, E. Ly, R. Lee, E. Mathiowitz, The effect of temperature and pressure on polycaprolactone morphology, Polymer (Guildf). 191 (2020) 122227. https://doi.org/10.1016/J.POLYMER.2020.122227.

[84] N.L. Leong, N. Kabir, A. Arshi, A. Nazemi, J. Jiang, B.M. Wu, F.A. Petrigliano, D.R. McAllister, Use of ultra-high molecular weight polycaprolactone scaffolds for ACL reconstruction, J. Orthop. Res. 34 (2016) 828–835. https://doi.org/10.1002/JOR.23082.

[85] D. Kołbuk, P. Sajkiewicz, T.A. Kowalewski, Optical birefringence and molecular orientation of electrospun polycaprolactone fibers by polarizing-interference microscopy, Eur. Polym. J. 48 (2012) 275–283. https://doi.org/10.1016/J.EURPOLYMJ.2011.11.012.

[86] A. Kienle, F.K. Forster, R. Hibst, Anisotropy of light propagation in biological tissue, Opt. Lett. Vol. 29, Issue 22, Pp. 2617-2619. 29 (2004) 2617–2619. https://doi.org/10.1364/OL.29.002617.